Cataloging and X-ray spectral analysis of supernova remnants in the M83 galaxy

Bachelorarbeit aus der Physik

eingereicht für den Erhalt des akademischen Grads Bachelor of Science

Maximilian Schroth

12. April 2022

Naturwissenschaftliche Fakultät
Dr. Karl Remeis-Sternwarte
Sternwartstraße 7, 96049 Bamberg
Friedrich-Alexander-Universität Erlangen-Nürnberg

Betreuerin: Prof. Dr. Manami Sasaki

I present a new supernova remnant (SNR) catalogue, with optical SNRs as reference objects and possibly X-ray and/or radio counterparts in M83. Processing data gathered in observations with the XMM-Newton telescopes resulted in 359 X-ray sources. The three different CCDs on the XMM-Newton spacecraft detected different numbers of sources. The MOS1 CCD detected 98, the MOS2 detected 129 and the PN CCD 132 sources. I compared the coordinates of all 359 X-ray sources with entries in my SNR catalogue to determine which of the detected sources are likely SNRs. Those XMM sources with counterparts in my SNR catalogue were plotted in optical images of the galaxy, showing that their positions mostly lie within the spiral arm structure of M83. Hardness ratios, progenitor masses and spectral characteristics of specific sources were analyzed in order to determine possible differences between remnants of thermonuclear supernovae (SNe) and remnants of core-collapse SNe. Twelve sources which show the highest X-ray emission between $0.7\,\mathrm{keV}$ and $1.1\,\mathrm{keV}$ were selected for further investigation based on their estimated progenitor star masses. Low star formation rates in the last $50\,\mathrm{Myr}$ surrounding the sources M2X110, M2X099 and M2X002 suggest they are good type Ia SNR candidates because they show no young progenitor. This is supported by the fact that the energy range of $0.7\,\mathrm{keV}$ up to $1.1\,\mathrm{keV}$ is expected to contain iron L-shell emission, often observed in the spectrum of remnants of thermonuclear SNe. Plotting and fitting spectra of source M2X007 and M2013 revealed two core-collapse SNR candidates with higher emission in harder X-rays.

Contents

1. Introduction

In this thesis, I developed a catalogue of supernova remnants (SNRs) located in the intermediate spiral galaxy called M83. Supernovae (SNe) are extremely luminous explosions of stars which sometimes can be observed by the naked eye if they are bright and close enough to earth. The explosions leave colorful structures behind, the so called supernova remnants.

The remnants featured in my catalogue can be compared to detected sources in the X-ray waveband based on data acquired by the XMM-Newton telescopes (XMM: X-ray Multi-Mirror Mission). During past observations of M83, other catalogues have already been developed, but those catalogues also contain astronomical objects other than supernova remnants. SNRs are generally bright X-ray sources, which lead to the choice of analyzing X-ray data for this project. The comparison of SNRs in my catalogue with the detected X-ray sources help determining which XMM sources are most likely supernova remnants.

Towards the end of my work, I will analyze the various different properties of those XMM sources, that I identified as SNR candidates (i.e. only sources that have counterparts in my catalogue). The examined properties include the positions of the sources within M83, their hardness ratios, counts as well as count rates and lastly their spectral characteristics. The results of this analysis will then be presented alongside a discussion based on previously gathered information about the structure of M83 and the nature of supernova remnants.

Regarding the structure of the galaxy, the most important aspect are its spiral arms, in which stars are believed to form more frequently than in other parts of spiral galaxies. Also the remnants of said stars are expected to be found mostly within these spiral arms, since their position should coincide with their respective progenitor star. Therefore, the coordinates of the supernova remnant candidates in the catalogue are crucial for the determination of the position of progenitor stars within M83. Within this thesis, all coordinates are given as right ascension and declination in the sexagesimal format with an epoch of J2000 and in the *fk5* system.

The spectral analysis will serve as a basis for the planned identification of X-ray sources either as the remnants of a core-collapse supernova (SN of type II) or those of a thermonuclear supernova (SN of type Ia). Beforehand, I aim to differentiate between the two types of supernovae based only on hardness ratio diagrams, without looking at the spectra. The counts belonging to the different XMM sources help determining, which of the detections could have the most reliable (statistically speaking) and most promising spectral data.

Core-collapse supernovae occur at the end of the lifetime of a massive star, whereas thermocunclear supernovae can often be observed in a binary system, composed of a still "living" star and a white dwarf, which accretes matter from the living star and is then driven to its own explosion.

2. Background about the M83 galaxy

M83 (NGC5236), also called the Southern Pinwheel Galaxy, is an intermediate spiral galaxy in the star constellation *Hydra* with its center located at $13^{\mathrm{h}}\,37^{\mathrm{m}}\,0.92^{\mathrm{s}}$ right ascension and declination of $-29°\,51'\,56.74''$ [11, 19]. The center of the galaxy and its nearest surroundings cover a circular area of about $0.5' \times 0.5'$. This area is also referred to as the nuclear region within this thesis. The whole galaxy measures approximately $8.3' \times 8.3'$ [9]. A picture taken in the optical band can be seen in Figure 1. M83 is a starburst galaxy, nearly face-on and does not have an active galactic nucleus (AGN) in its center. The nearly face-on characteristic allows to observe the structural properties of the galaxy very precisely compared to galaxies whose galactic plane is tilted away from the field of view.

The two main spiral arms of M83 originate from the nuclear region or the so called bar of the galaxy, even though this bar is not as distinctive as for barred spiral galaxies (which lead to the SAB classification) [11]. Several smaller spiral arms are connected to the main arms, especially visible in the upper right of the image [11]. In the arms of spiral galaxies, the star population is generally very young and the stars can be found even in the outmost fringes of the arms. Presumably, the "Pinwheel" part of the galaxy's nickname is inspired by the structure of M83. "Southern" was added due to the southern position of M83 between $-29°$ and $-30°$ declination [11].

Figure 1: An optical image of M83 taken by Johannes Schedler. Notice the bright nuclear region and the clearly visible spiral arms. Image taken from [11].

3. Stellar evolution

Before the development of any catalogue and doing following analysis, it is important to get an overview about the main object of interest, the supernova remnants. Supernova remnants are the remainders of explosions of stars, the supernovae. In order to better comprehend the temporal evolution of SNe and SNRs, this chapter will start with a summary of the basic stellar evolution. Note here, that this summary and the description of the time evolution of a SNR are not very detailed, since this is not the main goal of the project, but there are nonetheless important facts, that need to be mentioned.

3.1. Basic stellar evolution and supernovae

The dominant process during the evolution of a star preceding the end stages is core fusion. At first, hydrogen is fused to helium, helium is then fused to form carbon and oxygen. Further fusions resulting in heavier elements are possible if the initial mass of the star is great enough. Gravitational forces compress the core of the star which provides the increase of pressure and temperature necessary for the fusion of heavier elements. In any case, the heaviest element that can be formed is of the iron-platinum-group, whose isotopes of elements have the highest binding energy per nucleon. Thus, from this point on, the fusion process would no longer be exothermic and no more energy can be released through core fusion. Energy resulting from fusion processes escapes the star as radiation and counteracts the gravitational force acting on the core of the star. When all fusion material is depleted, radiation energy and resulting forces can no longer withstand the gravitational pressure of the star. Now, further stellar evolution depends on the initial mass of a given star. The star can take different ways of evolution. Two of them shall be described in more detail here.

Stars with end masses below the Chandrasekhar limit ($1.44\,M_\odot$) become white dwarfs. As stated above, the possible fusion processes in the star depend on the initial mass of the star, which measures up to $\approx 8\,M_\odot$ for stars evolving into white dwarfs. In stars that do evolve into white dwarfs, no elements heavier than carbon and oxygen can be formed. After fusion stops, the star collapses under its own gravitation and will be compressed until no further compression is possible due to the Pauli principle. The collapse is haulted by the degenerate electron pressure. The white dwarf has approximately the mass of our Sun and the size of our Earth and will cool down further. White dwarfs are often part of a binary system consisting of an additional, living star. Studies of SNe have shown that most supernovae of type Ia have similar properties, such as light curves and optical characteristics. This suggests similar initial conditions for all those SNe. Most white dwarfs at the Chandrasekhar limit have similar properties and thus could be the constant starting points of thermonuclear SNe. Since white dwarfs are stable, it would need further mass to surpass the Chandrasekhar limit. This mass can be provided by the second star in the binary system and is accreted onto the white dwarf. The additional mass causes the degenerate electron pressure to fail to counteract gravitational forces.

Temperature rises and the original end products in the heart of the star, carbon and oxygen, can now fuse, resulting in an explosive wave. The explosion propagates first through the core of the star and in the end completely disrupts it in a supernova of type Ia [18].

Stars of end masses greater than $3\,M_\odot$ can evolve beyond this point to either become a neutron star or a black hole (BH). Those stars have initial masses of more than $\approx 10\,M_\odot$. Their general evolution is similar to the one leading to white dwarfs, only they are more massive at the beginning and heavier elements, such as neon, sulphur and silicon, can be formed, which leaves the well known onion-like shell structure of the star with iron in its core behind. The core is stabilized by degenerate electrons. As stated above, no element (isotope) heavier than iron can be formed (mostly ^{56}Fe, an isotope of iron with one of the highest binding energies per nucleon of all elements and isoptopes of elements). Even though iron in the core can no longer fuse heavier elements, the layers surrounding the core are still able to go through fusion processes, ultimately creating more iron. As a result, the temperature and the pressure in the core start to rise. Now, free protons created by photodesintegration of iron nuclei capture electrons to form neutrons and neutrinos. Because of the loss of these electrons, further gravitational collapse of the star cannot be haulted by degenerate electrons but instead by the degeneracy of neutrons. Gravitational collapse happens extremely fast and the graviational forces are enormous. Before further collapse can be diverted, the core collapses under its own gravitation and outer layers of the star begin to fall onto the core. This creates a shock wave leaving the star, propelling the outest material away from the star, resulting in a core-collapse (type II) supernova [18]. Further evolution of the star into a neutron star shall not be discussed here. Instead, the following subsection addresses important characteristics of remnants of supernova explosions.

We observe the remainders of a supernova as a colorful structure, such as the famous Cassiopeia A (Cas A) or the remnants of Tycho's SN1572 (B Cas) shown in Figure 2 and Figure 3, respectively. The structures can have various different shapes and colors. Those structures are called supernova remnants (SNRs).

3.2. Supernova remnants

They are produced by a shock wave distributing fused material (ejecta) from the progenitor star in the interstellar medium. The interstellar gas is heated to temperatures of 10^6 K to 10^7 K (which can be compared to the temperature of the Sun's corona). This thermal plasma can be observed in X-rays, although young supernova remnants also emit non-thermal X-rays. Supernova remnants are also bright in radio. In the optical, supernova remnants often show strong [O III] and [S II] emission lines, but also [O I] and [N II] [17]. Those emissions correspond to so called forbidden transitions. Electrons that make transitions from one quantum state to another, release energy in the form of radiation. But not all transitions are possible because electrons obey certain selection rules for transitions. A change in the quantum state that is fully described by the four quantum

Figure 2: Supernova remnant Cassiopeia A (Cas A), probably of a type II SN [18]. Image taken from [6].
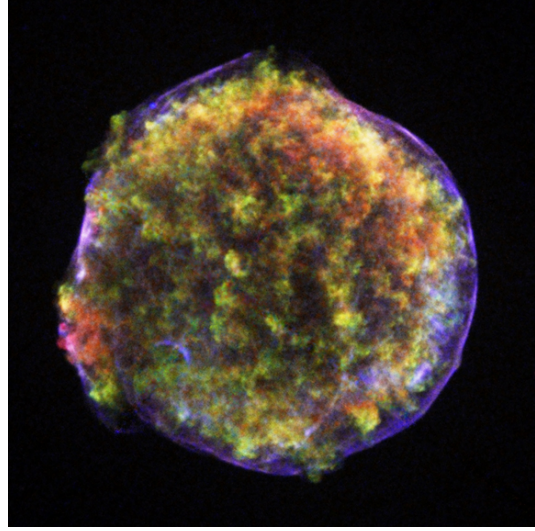
Figure 3: Tycho's supernova remnant (B Cas) of SN1572, a type Ia SN [18]. Image taken from [24].

numbers, the principal quantum number n, the angular momentum quantum number l, the magnetic quantum number m and the spin quantum number s, requires a change in at least one of those quantum numbers. Transitions with a difference of $\Delta l = \pm 1$ in the quantum number l for instance are referred to as allowed transitions, whereas transitions with $\Delta l \neq \pm 1$ are called forbidden transitions [5].

The time evolution of supernova remnants can be separated into four phases. The free expansion followed by the Sedov phase, the radiative phase and finally the merging phase [17].

During the free expansion (lasts $\approx 100\,\mathrm{yr}$), the ejected material from the preceding supernova expands and sweeps up the interstellar medium. In this phase, the temperature in the supernova remnant and the expansion velocity of the shell of the SNR are constant. If more and more matter in the ISM is swept up by the shock wave of the SN, this marks the beginning of the Sedov phase (also called adiabatic phase, $10 \times 10^3\,\mathrm{yr}$ to $20 \times 10^3\,\mathrm{yr}$). The shock wave interacts with the ISM, creating an additional, inwards-directed shock wave (the reverse shock). The shell of the supernova remnant breaks into clumps because of its Rayleigh-Taylor instability. Due to turbulence, the ejecta of the SNR gets mixed up with the gas in the interstellar medium that was just shocked by the outer shock wave. After that, the shell cools down to about $5 \times 10^5\,\mathrm{K}$ and enters the radiative or snowplough phase ($\approx 10^5\,\mathrm{yr}$). Electrons recombine with heavier atoms, which leads to UV (ultraviolet) and optical emission mentioned above, radiated by the shell of the SNR. As a result, the cooling down process of the shell is fastened, making it shrink and become more dense. The merging phase marks the end of a SNR. The shock velocity behind

the shock becomes comparable to the turbulent velocity and the temperature similar to the temperature of the surrounding ISM. The SNR decreases in brightness and becomes slowly indistinguishable from the interstellar medium [17].

Research has been done on the spectral properties of supernova remnants (namely on differences betweeen remainders of core-collapse and thermonuclear SNe), for example by Kavanagh et al. [10]. In their publication in Figure 9, they report the spectrum of two supernova remnants in the Large Magellanic Cloud (LMC). Both of the sources showed significantly high Fe L-shell emission, suggesting SNe of type Ia [10]. Later on in my project, I want to evaluate and compare the spectral properties of two SNR candidates in M83 with the analysis of Kavanagh et al. In addition to the spectrum, I aim to look for hints at either type Ia or core-collapse SNe also in the hardness ratio diagrams.

4. Development of the SNR catalogue

During the first part of my work, I developed a catalogue of supernova remnant candidates. The catalogue can later be used in order to compare its entries to X-ray detections of the XMM-Newton telescopes. The different entries in the catalogue contain information on two important properties of a supernova remnant: its coordinates and in which waveband the counterparts of the optical SNR were observed.

4.1. Catalogues in literature

Before the development of the catalogue, I looked into four previously published papers on spectral properties of supernova remnants (and other objects) in M83. The authors of two of these papers used X-ray observations (Ducci et al. [9], Long et al. [12]), one optical (Winkler et al. [27]) and one radio observations (Russel et al. [15]) for their analysis and discussion. Later on, I used all of these four catalogues for cross-correlations in order to develop my own catalogue of SNR candidates.

Winkler et al. performed follow-up spectral analysis and source identification based on data gathered by Blair et al. (2012) [3] with the Magellan/IMACS telescope (notes on spatial resolution: $0.11''$ per pixel, seeing of $0.4''$ to $0.5''$ [3]) as well as by Dopita et al. (2010) [8] and Blair et al. (2014) [4] with the Hubble Space Telescope/WFC3 (note on spatial resolution: $0.06''$ at Hα [8]). This analysis resulted in 118 optical sources, of which 117 were classified as supernova remnants based on their [S II] to Hα emission ratio. 22 further optical sources were selected as SNR candidates based on their [O III] to Hα ratio. Only two of those were confirmed as SNRs. The other 20 were either not definitely classified or classified as sources other than SNRs. It shall be noted here, that Blair et al. published two corrections ([2, 1]) on their paper from 2012, mainly affecting previous calculations of fluxes, but no significant changes to the coordinates of sources were reported. Only after the second correction, the position of one source (B12-014) was slightly corrected [1].

A second catalogue containing optical SNRs was published by Russel et al. However, they also did not detect these sources themselves. Instead, they performed forced photometry by integrating radio data at the positions of known optical SNRs listed in the catalogue by Williams et al. [15, 26]. The radio data from Russel et al. was obtained via the Australia Telescope Compact Array (ATCA, spatial resolution: $3.2'' \times 1.4''$ [15]), which detected 270 radio sources. In addition to the mentioned optical forced photometry, Russel et al. also executed X-ray forced photometry in the same manner based on X-ray data from Long et al. [15]. Through the forced photometry, not all Long et al. X-ray sources are featured in the Russel et al. X-ray catalogue, but only 378.

Long et al. detected in total 458 X-ray sources with Chandra (spatial resolution: $0.5''$ [7]). This data is supported by ATCA observations of M83, resulting in 109 radio sources.

Lastly, Ducci et al. used the XMM-Newton telescopes (spatial resolution: $6''$ [22]) to perform X-ray studies on M83 and detected 189 sources.

4.2. Naming conventions

One main outcome of the analysis in all four papers were observation specific catalagues. These catalogues contain the identifiers of astronomical objects and their coordinates. The identifieres (IDs) have different naming conventions, mostly depending on the waveband in which the objects were observed or the year of detection.

Optical IDs in the Winkler et al. paper start with either "B12-", "B14-" or "D10-", followed by a number, which is just the number of the source. B12 is the first letter of the first named author in Blair et al. (2012) and the year of publication. The same naming concept resulted in B14, corresponding to sources reported in Blair et al. (2014) and D10, marking sources featured in Dopita et al. (2010). Examples: *B12-312*, *B14-09* or *D10-N-17*. The last source is not to be confused with *D10-17*, which is another source. The "N" in the middle of the ID underlines the fact that it lies within the nuclear region.

The identifiers of the sources reported in Williams et al. (that were used for the forced photometry by Russel et al.) align with the Winkler et al. IDs, because their analysis was based on the same data. Radio sources detected by Russel et al. start with an "R" for radio, followed by a "20" (observations were done in 2020) and again the number of the source. Thus, the first source is called *R20-001* and the last one *R20-270*. X-ray sources have the same names as the identifiers used in Long et al.

Radio identifieres in the Long et al. catalogue start with an "A" (presumably standing for "ATCA"), followed by a number, which is once more just the number of the source. So, first object: *A001*, last object: *A109*. The X-ray sources start with an "X" for X-ray and end with the number of the source. The first source is then called *X001* and the last one *X458*. Hereafter, they are named *CX001* to *CX458* ("C" for Chandra) in this work, to avoid confusion with Ducci et al. X-ray sources.

Ducci et al. reported 189 X-ray sources, that all simply carry the number of detection as their name, without any special additional letters. To avoid confusion with other numericals, an "X" is added to the beginning of the identifier. So the first source is *X001* and the last one is *X189*.

4.3. Cross-correlations

Each one of the catalogues was later cross-correlated with other already exisiting catalogues and the coordinates of objects therein, in order to possibly identify the type of the astronomical object. However, none of the authors published an entire catalogue with information solely on supernova remnants in the three wavebands, that I am mainly considering from this point on: X-rays, radio and optical. The cross-correlation of Ducci et al., Long et al., Winkler et al. and Russel et al. also include the positions of other detections, i.e. other astronomical objects such as stars, X-ray binaries (XRBs) or active galactic nuclei (AGNs) of other galaxies. A list of exclusively supernova remnants however, is more suitable for the analysis done in this project.

Thus, I performed additional cross-correlations between the four catalogues myself, which resulted in a list of 299 optical supernova remnant candidates and possibly X-ray or/and radio counterparts (and their coordinates as well). The remnants observed in the optical waveband served as a reference for the cross-correlation. Winkler et al. published a list of such optical SNRs, that were either selected because of their prominent [S II] to Hα ratio or prominent [O III] to Hα ratio. Russel et al. performed forced photometry by integrating their radio detections at the positions of known optical supernova remnants. The positions of optical SNRs were based on data analyzed by Williams et al., whose data was in turn also based on the work of Blair et al. from 2012 and 2014 and of Dopita et al. in 2010.

So there were now two sets of optical supernova remnants and SNR candidates to choose from. I decided to take the coordinates from Russel et al. as references, because there were more SNRs compared to the other optical data set. Plus, sources from Winkler et al. align with those in the catalogue from Russel et al. Yet, some sources are only reported in the work of Russel et al. and Williams et al., but not in the one by Winkler et al.

The cross-correlations between optical, radio and X-ray sources were simplified a little bit, since Russel et al. also did the cross-correlations between their own catalogues. Therefore, filtering for only those sources that are supernova remnants or supernova remnant candidates and additional cross-matching of optical sources in Russel et al. with the X-ray sources in Long et al. was required. The cross-matching was done as an additional check-up and as expected only yielded matching identifiers. Long et al. X-ray sources in my catalogue were mostly already classified as SNRs. Some were not yet classified, but since they align with optical and possibly radio sources, it is likely, that they indeed are supernova remnants. Three sources are believed to be unlikely SNRs in the Long et al. catalogue, but since these are only candidates and not certain

classifications, I included them in my catalogue nevertheless. Radio sources from Long et al. were also included, if the X-ray hardness suggests that the corresponding source is a supernova remnant [12]. Lastly, I correlated the optical sources with the Ducci et al. X-ray sources. In contrast to the Long et al. sources, they generally do not have the same identifier and not all Long et al. sources were also detected by Ducci et al. and vice versa because different telescopes (detectors) were used for the observations. In the catalouge, sources with several counterparts in other wavebands are more likely to be undoubtedly supernova remnants than sources with fewer or no counterparts, since the identification can then be based on more data. The above mentioned correction of the position of source B12-014 did not result in any changes regarding the cross-correlation.

Several sources are located in or nearby the nuclear region of the galaxy. This makes it difficult to correlate the sources in X-ray and radio with the optical supernova remnants because of confused emmision originating from the center of M83. Nonetheless, I attempted to cross-match the sources and added a *nuc* (nuclear) flag to denote sources that lie in the nuclear region. Additional difficulties arise because of limited spatial resolution of detectors and telescopes. The consequence of the use of *nuc* flags is the fact, that some optical reference sources have the same counterpart in my catalogue. Not only do some optical sources have the same counterpart, but because of spatial resolution and confused emission from the nuclear region, some optical SNR candidates also have more than one reported radio counterpart.

Furthermore, within my catalogue and the following analysis, I distinguish between *optical_s2* and *optical_o3*, meaning either [S II]- or [O III]-selected supernova remnants, if known. This corresponds to the classification of Winkler et al. mentioned earlier.

4.4. Historical Supernovae hosted by M83

The catalogue contains the coordinates of the remnants of two historical supernovae, that were detected within the last 100 yr. SN1923A (B14-58) and SN1957D (B12-324) with the identifiers of their remnants in parentheses [15]. The object B12-174a has no specific SN identifier in terms of naming convention of supernovae because it was actually not detected but its remnants were recently discovered [15] and can also be found in the catalogue under the identifier B12-174a.

The remnant R20-064 of one more supernova (SN1950B) was detected by Russel et al., but only in the radio waveband and thus has no entry in my catalogue because it has no optical counterpart, that I chose as references.

The supernova SN1968L was not reported to have a remnant with radio emission in Russel et al. but its remnants were probably detected by Long et al. as SNR CX216. This X-ray emission is also featured in my catalogue as the counterpart of the optical SNR D10-N-05, although it lies in the confused nuclear region. Dopita et al. carried out an optical observation of this nuclear region and also found a candidate for the remnants of SN1968L based on the [O III] to Hα ratio.

SN1945B and SN1983N are the remaining two supernovae observed in the last century in M83. Their remnants were however not detected in either waveband in any of the four publications I consulted for the development of my own catalogue.

See Table 1 for a combined list of all mentioned historical supernovae. Table 2 lists the known remnants of the above mentioned supernovae, except for SN1945B and SN1983N, which do not have associated objects in my catalogue. The position of all seven supernovae can be seen alongside the position of the catalogue entries in Figure 4.

4.5. Own catalogue

A short excerpt from the catalogue can be seen in Table 3, while the entire catalogue can be found in Appendix A. The catalogue contains the identifier of the optical SNR candidate according to Russel et al. in the first column, followed by its coordinates in the second column. Depending on which and how many counterparts an optical source has, the next columns list these counterparts and their respective coordinates. The third column gives the X-ray IDs of the counterpart. The coordinates of the X-ray counterpart are in the fourth column. Radio IDs are found in column five and its coordinates in column six. The last column consists of informative flags on the optical source and whether the source lies in the nuclear region. The flag *s2* means optical sources were chosen as SNR candidate because of the [S II] to Hα ratio and the flag *o3* means they were chosen because of their [O III] to Hα emission ratio. If neither of the two flags above is present, it is not reported in Winkler et al., based on which emission ratio the optical SNR was chosen. The flag *nuc* is only added, if the source lies in the confused nuclear region. Note here, that not all sources have the same amount of counterparts. Optical sources, that do not have any match within the catalogue, are less probable to be SNRs, but it is nonetheless still possible. As the result of including those optical SNR candidates, there are quite a few sources in the entire catalogue without any counterparts.

For visual presentation, the catalogue entries are also plotted in an optical image generated by SkyView [20] in Figure 4. The green "Xs" represent the coordinates of all optical SNR candidates from Russel et al. It is already discernible here, that the green "Xs" and thus the optical SNRs mostly follow the structure of the spiral arms of the M83 galaxy, but also that the remnant candidates in the inner regions are more densely distributed than in the outer regions. This can be explained by the lower star formation (SF) rate in the outer regions ($10^{-5} \, M_\odot \, \mathrm{y}^{-1}$) compared to the SF rate in the inner regions ($\approx 10^{-2} \, M_\odot \, \mathrm{y}^{-1}$) [11]. Blue boxes denote the historical supernovae in accordance with Table 1. The overlap between four of the seven supernovae, which have reported optical remnants in Table 2, can clearly be seen.

Table 1: List of seven historical supernovae followed by their respective coordinates. Their remnants in the optical (if detected) and the coordinates of the remnants are also given. The coordinates of the SNe were taken from *SIMBAD* [19], except for SN1945B, because the coordinates in *SIMBAD* are ill-defined. The coordinates of this SN are taken from *NED* [14].

SN	RA (h,min,s) DEC (h,′,″)	SNR (optical)	RA (h,min,s) DEC (h,′,″)
SN1923A	13 37 09.20 −29 51 04.0	B14-58	13 37 9.31 −29 50 58.5
SN1945B	13 36 51.00 −29 54 56.0		
SN1950B	13 36 52.88 −29 51 55.7		
SN1957D	13 37 03.57 −29 49 40.7	B12-324	13 37 3.58 −29 49 40.7
SN1968L	13 37 00.42 −29 51 59.8	D10-N-05	13 37 0.39 −29 51 58.7
SN1983N	13 36 51.23 −29 54 01.7		
B12-174a	13 37 06.64 −29 53 32.7	B12-174a	13 37 6.65 −29 53 32.6

Table 2: List of objects associated with optical supernova remnants of seven historical SNe that occured in the last 100 years.

SN	optical SNR	associated object
SN1923A	B14-58	R20-228
SN1950B	-	R20-064, A024
SN1957D	B12-324	X279, R20-172
SN1968L	D10-N-05	X216
B12-174a	B12-174a	X316, R20-193
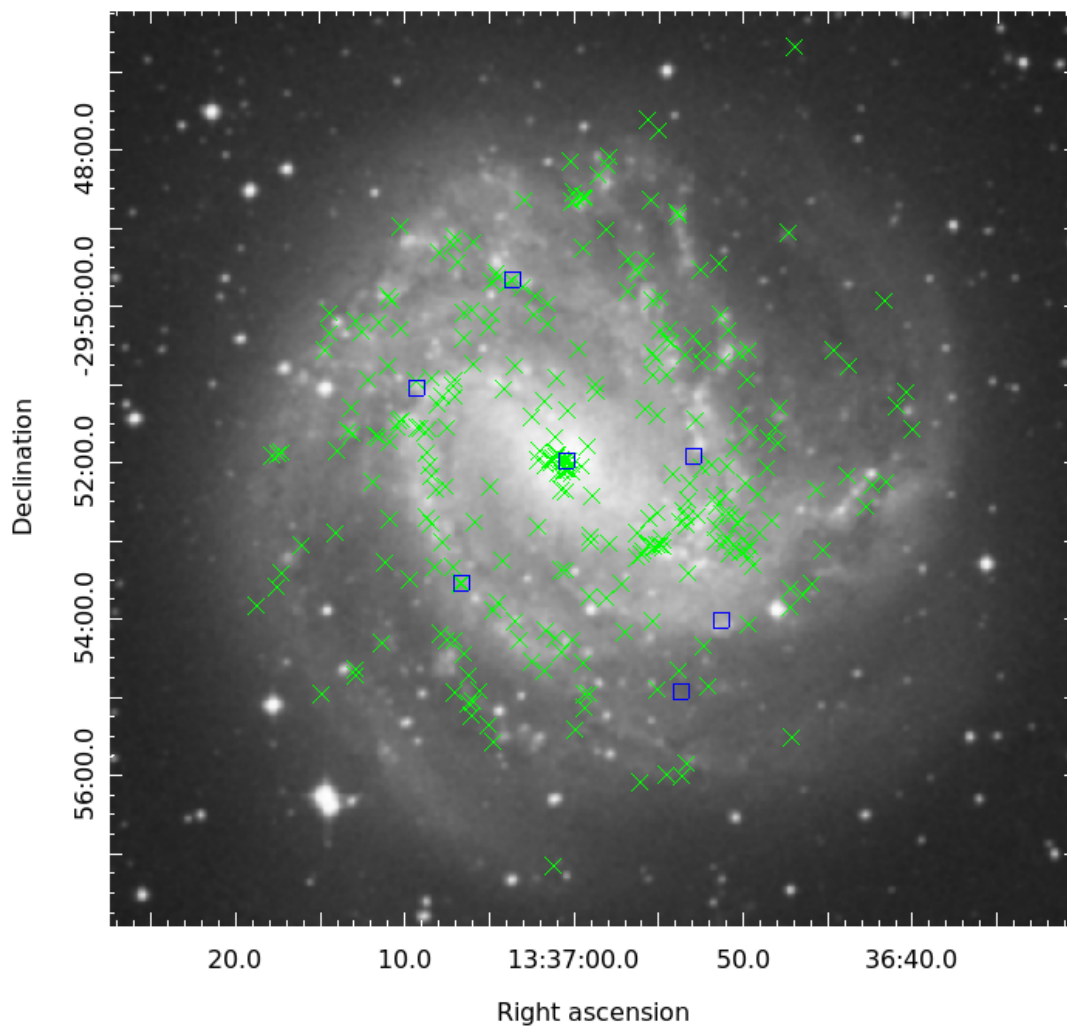
Figure 4: An optical image of M83 taken from [20] (Digitized Sky Survey, image size: 1200 pixels and 0.33°). The green "Xs" represent the optical sources reported in Russel et al. [15]. Blue boxes denote the historical supernovae according to Table 1.

Table 3: Short excerpt from the SNR catalogue with optical references and coordinates, X-ray counterparts and coordinates, radio counterparts and coordinates as well as the informative flag column. See Appendix A for the entire catalogue.

optical	RA (h,min,s)			DEC (h,','')			X-ray	RA (h,min,s)			DEC (h,','')			radio	RA (h,min,s)			DEC (h,','')			flags[a]
B12-001	13	36	39.99	−29	51	35.10															s2
B12-002	13	36	40.35	−29	51	6.52	X055	13	36	40.73	−29	51	9.10								s2
B12-003	13	36	40.90	−29	51	17.71	CX019 (M1X047)	13	36	40.87	−29	51	17.80	R20-008	13	36	40.90	−29	51	17.80	
B12-004	13	36	41.50	−29	52	15.89															s2
B12-005	13	36	41.58	−29	49	56.32															
B12-006	13	36	42.33	−29	52	17.40															s2
B12-007	13	36	42.72	−29	52	35.00								R20-015	13	36	42.73	−29	52	35.40	
B12-008	13	36	43.70	−29	50	45.89															
B12-009	13	36	43.82	−29	52	11.21															s2
B12-010	13	36	44.64	−29	50	33.90															s2
B12-011	13	36	45.31	−29	53	7.80															
B12-012	13	36	45.66	−29	52	21.29															s2
B12-013	13	36	45.93	−29	53	34.40															
B12-014	13	36	46.42	−29	53	42.29															s2
B12-015	13	36	46.94	−29	46	41.70															
B12-016	13	36	47.13	−29	55	31.51															
B12-017	13	36	47.18	−29	53	51.40															
B12-018	13	36	47.22	−29	53	36.89															
B12-019	13	36	47.30	−29	49	3.79															
B12-020	13	36	47.83	−29	51	18.11															s2
B12-021	13	36	47.93	−29	51	46.01															s2
B12-022	13	36	48.11	−29	51	33.91															s2
B12-023	13	36	48.30	−29	52	44.69	CX046	13	36	48.30	−29	52	44.60								s2
B12-024	13	36	48.45	−29	51	42.19															s2
B12-025	13	36	48.59	−29	52	5.30															s2
B12-026	13	36	48.99	−29	52	54.08	X069 (M2X008)	13	36	49.07	−29	52	58.70								s2
B12-027	13	36	49.12	−29	52	24.89															
B12-028	13	36	49.37	−29	53	19.90															
B12-029	13	36	49.54	−29	51	37.12								R20-030	13	36	49.35	−29	51	36.30	s2
B12-030	13	36	49.60	−29	53	5.71															
B12-031	13	36	49.62	−29	53	13.70															s2
B12-032	13	36	49.63	−29	50	34.40															s2
B12-033	13	36	49.68	−29	54	4.21															s2
B12-034	13	36	49.72	−29	50	57.08															s2
B12-035	13	36	49.81	−29	53	8.30															s2
B12-036	13	36	49.81	−29	52	16.90	CX053	13	36	49.80	−29	52	17.20								s2
B12-037	13	36	50.12	−29	53	8.70	CX057	13	36	50.09	−29	53	8.40	R20-035	13	36	50.12	−29	53	8.80	
B12-038	13	36	50.23	−29	51	24.30															
B12-039	13	36	50.28	−29	52	47.50															s2
B12-040	13	36	50.50	−29	51	49.79															
B12-041	13	36	50.55	−29	53	3.91	CX061	13	36	50.59	−29	53	3.80								

[a] *s2:* optical SNR was chosen because of the [SII] to Hα ratio, *o3:* optical SNR was chosen because of [OIII] to Hα ratio, *nuc:* source lies in the nuclear region of M83

5. XMM-Newton data

5.1. XMM-Newton telescopes

Before getting to the actual data processing, I first want to give a short introduction to the CCD Cameras carried by the *XMM-Newton* spacecraft. The X-ray Multi-Mirror Mission (XMM) consists of three different telescopes, each of which carries an X-ray CCD array. The arrays are two MOS (MOS1 and MOS2, MOS meaning Metal Oxide Semi-conductor) and one PN camera. Those three cameras as a whole form the European Photon Imaging Camera (EPIC). The two MOS CCDs are mounted orthogonally to one another on the spacecraft. The construction of the spacecraft as well as the location of the EPIC instruments and their corresponding X-ray telescopes on the spacecraft cause different ratios of incoming beam fluxes and the beam fluxes detected by the CCDs. The beam of the telescope corresponding to the PN camera is not diverted by any other instrument and as a result, naturally higher count numbers detected by the PN CCD array are expected compared to the MOS CCDs [22]. X-ray beams detected by the two MOS cameras are partially diverted away to be utilized by the Reflection Grating Spectrometers (RGS) [23]. The names of the two types of cameras already hint at the differences in their design. They also show different geometry as well as physical properties affecting the way the incoming X-rays are processed, such as readout times. The PN camera is more sensitive than the other two cameras, whereas the MOS CCD arrays have the higher spectral resolution [22].

In general, EPIC instruments work under the principle of photon counting mode. The attributes of detected sources then include, amongst others, the arrival time of the photons, their energies and their positions on the detectors. The attributes are collected in event lists, where one entry line is associated with the attributes of a single event [22]. The event files will contain the necessary data for my discussion of X-ray properties of supernova remnants. The total angular resolution of the telescope measures $6''$ and covers an energy range of $0.15\,\mathrm{keV}$ up to $15\,\mathrm{keV}$ [22]. However, the energy bands chosen for the analysis in this project are $0.3\,\mathrm{keV}$ - $0.7\,\mathrm{keV}$, $0.7\,\mathrm{keV}$ - $1.1\,\mathrm{keV}$ and $1.1\,\mathrm{keV}$ - $4.2\,\mathrm{keV}$, confining the total energy range from $0.3\,\mathrm{eV}$ to $4.2\,\mathrm{eV}$.

Those three energy bands are expected to contain the most informative and most promising data when it comes to the thermal spectrum of a SNR. The softest band from $0.3\,\mathrm{keV}$ up to $0.7\,\mathrm{keV}$ is believed to contain strong oxygen emission lines. Amongst others, the middle band includes the Fe L-shell line and the hard band consists of lines from heavier elements such as magnesium, silicon, sulphur, carbon and argon and possibly non-thermal continuum. The thermal spectrum represents the spectral characteristics of a given SNR and can be used for the evaluation based on the band, in which the emission by the supernova remnant is prominent. High numbers of counts in the softest band suggest cool objects, while (young) objects with hot components or non-thermal emission also have significant emission in the hard band [13, 10].

5.2. Observation data

By looking at various different physical quantities derived from the event files, such as positions of detected sources, hardness ratios, counts as well as count rates and extracted spectra of specifically selected detections (find more information on the selection process in subsection 6.5), I want to evaluate the differences between thermonuclear supernovae and core-collapse supernovae. The data used within the scope of this project were taken in an observation with XMM that was already completed before I started this analysis. The observation files can be found in and downloaded from the *XMM-Newton Science Archive Search* [28]. Several different observations of M83 done in the past are available on this website. I selected the observation *0761620101* performed on August 7, 2015, since there is fewer background noise from the Sun's particle radiation compared to other observations. The observation was not pointed directly to the center of M83, but to $13^{\rm h}\,37^{\rm m}\,05.12^{\rm s}$ right ascension and a declination of $-29°\,52'\,7.0''$. The center of the galaxy is at $13^{\rm h}\,37^{\rm m}\,0.92^{\rm s}$ and $29°\,51'\,56.74''$ according to *SIMBAD* [19].

6. Data processing and analysis

6.1. Processing

In order to process the downloaded data from the selected observation, I used an analysis module named `xmmsas`, which I could access via the computers at the local Remeis observatory in Bamberg (institution belonging to the Friedrich-Alexander-Universität Erlangen-Nürnberg). The team of XMM-Newton provide threads on how to best process and analyze the XMM data on their web page [16]. The threads I used included the *SAS start-up*, *event list generation*, *filtering against high background*, *EPIC source finding in one go via* `edetect_chain` and *spectrum extraction*. The exact commands can be found in Appendix B (some commands presented in the threads were slightly changed to make them applicable for my project).

The *SAS start-up* required the directories of the module and the calibration files to be able to properly process the data. The *event list generation* produced the initial event files for each camera separately. The methods in *filtering against high background* accounted for irregularities due to undesired high particle background in the detections and ultimately yielded the cleaned event files *<camera>clean.fits*, where "camera" is either MOS1, MOS2 or PN. Via `evselect` (a module designed for event selections), I managed to generate images of M83 for each camera in each energy band. The program `edetect_chain` used the cleaned event files and the images in all energy bands as references, detected the sources and produced the final list of detections for each CCD array.

Table 4: The energy conversion factors (ecf) in the three energy bands for the PN and the two MOS cameras.

	0.3 - 0.7 keV	0.7 - 1.1 keV	1.1 - 4.2 keV
PN (thin filter)	10.22	8.87	5.62
MOS (thin filter)	1.75	1.79	2.02

During the source detection in previously generated images of M83 for MOS1, MOS2 and PN, energy conversion factors (ecf) were needed. Within the examplary commands of the `xmmsas` thread, these conversion factors were used specifically for the examplary energy bands. Since I used different energy bands, I required different energy conversion factors. Those factors can be determined by regarding a given type of emission, simulating its spectrum and checking for the count rate of EPIC within this simulation. Instead of looking at the response matrices of EPIC and modeling a spectrum, I used the web-tool *WebPIMMS* for simplicity [25]. This tool converts fluxes (in units of $1 \times 10^{-11} \, \mathrm{erg \, cm^{-2} \, s^{-1}}$) into XMM counts per second. A typical spectrum for supernova remnants is an APEC model (APEC: Astrophysical Plasma Emission Code) for thermal plasma with a temperature of $k_{\mathrm{B}}T = 0.4846 \, \mathrm{keV} \approx 0.5 \, \mathrm{keV}$. Taking the foreground absorption by the interstellar medium in the milky way in the direction of M83 into account for the spectral model, results in a multiplicative component of $N_{\mathrm{H,Gal}} = 6 \times 10^{20} \, \mathrm{cm^{-2}}$ to be included in the calculation. Its value can be obtained by using the module `nh`, with an epoch of J2000 and the coordinates of M83 in the sexagesimal format $13^{\mathrm{h}} \, 37^{\mathrm{m}} \, 00.919^{\mathrm{s}} \, -29° \, 51' \, 56.74''$ (taken from *SIMBAD* [19]). The web-tool yielded the values featured in Table 4. Those factors could then be plugged into the commands related to the data processing.

6.2. Comparison of XMM sources with catalogue entries

The source detection in M83 images of all three cameras resulted in a list of X-ray sources for all three CCDs respectively. MOS1 detected 98 sources (*M1X001* to *M1X098*), MOS2 129 sources (*M2X001* to *M2X129*) and PN detected 132 sources (*PNX001* to *PNX132*). The X-ray sources could then be compared to my own catalogue containing the positions of optical supernova remnant candidates (and possible counterparts in other wavevands). Through this comparison, I examine only those detected sources further, that have counterparts in my list and thus are more likely supernova remnants. Note here, that in general, the ID of the MOS2 source is listed in the SNR catalogue as X-ray counterpart of the optical SNR candidate, if the position of the detections of the other two CCDs coincide with the one from MOS2. Only if a source was detected exclusively by MOS1 or PN, their respective IDs are given. I shall also point out, that the term counterpart is used in two different manners: Firstly, the counterparts of sources detected by XMM found in my catalogue. Secondly, these counterparts themselves have counterparts within the catalogue, which was described during the development of the catalogue in section 4.

I plotted the coordinates of both the sources detected by XMM and the objects in my catalogue in `ds9` for each imaging camera seperately. The XMM sources are not actually circles (they are rather point-like with a certain extension) but I plotted them as the center of circles with radii of both $R_6 = 6''$ (angular resolution of XMM) and $R_{12} = 12''$ (two times the angular resolution of XMM), taking positional errors into account. Using the sources as circular regions, I could classify the kind of overlap between a given object in my catalogue and a given detected source. For one thing, there are counterparts in my catalogue within a $6''$ radius surrounding an XMM source or within a $12''$ radius. For another, I also had to distinguish between counterparts with coordinates arbitrarily close to the R_{12} circle and counterparts that lie way outside of this circle. "close" was not further specified, so this choice was based on my judgement of "close proximity" on an astrophysical scale alone. This later turned out to be irrelevant, since choosing objects that even lie in the R_{12} circle as counterparts of XMM sources was a rather unfortunate choice to begin with because the radius was chosen too big. I further elaborate on this problem in subsection 6.5.

For each of the three cameras, the comparison in `ds9` resulted in a region file of coordinates of XMM sources. Merging those region files and plotting them in `ds9` yielded a collection of XMM sources in Figure 5. The merged region file contains information on the type of the counterpart (optical and/or radio) and with which CCD array the source was detected. Boxes correspond to MOS1, circles to MOS2 and crosses to PN. Lots of sources were detected by more than one camera. The symbols can therefore overlap. The regions are also color-coded, such that it can be distinguished between the type of counterpart visually as well. Green regions are sources with counterparts selected because of their [S II] to Hα ratio (referred to as *optical_s2*) while blue regions have counterparts with either prominent [S II] to Hα ratio or [O III] to Hα ratio (which will be referred to as *optical*). Regions in cyan and magenta also have counterparts in *optical_s2* and *optical*, respectively, but both additionally have radio counterparts.

Lastly, the regions have an additional criterion, namely if HR_1 and HR_2 are positive or negative. I further elaborate on the hardness ratios in subsection 6.3. The HRs correspond to the different HRs collected by the given camera. This is the reason, why one single source detected by multiple cameras does not always show the same hardness ratio for each camera.

The detected sources mostly lie within the spiral arms of M83, which matches the previous assumption of the location of remnants, since the star population in the galaxy is concentrated mostly in the spiral arms. Even in the outmost regions of the galaxy, supernova remnants can be found. The remarks on the distribution of the remnants made for Figure 4 also hold for the distribution of the sources detected by XMM.

Out of the remnants of the seven historical supernovae, none coincides with a detected source in X-ray in Figure 5. The remnant of SN1968L seems to have a counterpart within the XMM sources, but as stated in section 4, this supernova occured in the confused nuclear region of M83. Thus, it is difficult to confirm this detection as X-ray emission coming from the remnant of SN1968L, even though Long et al. could have found an
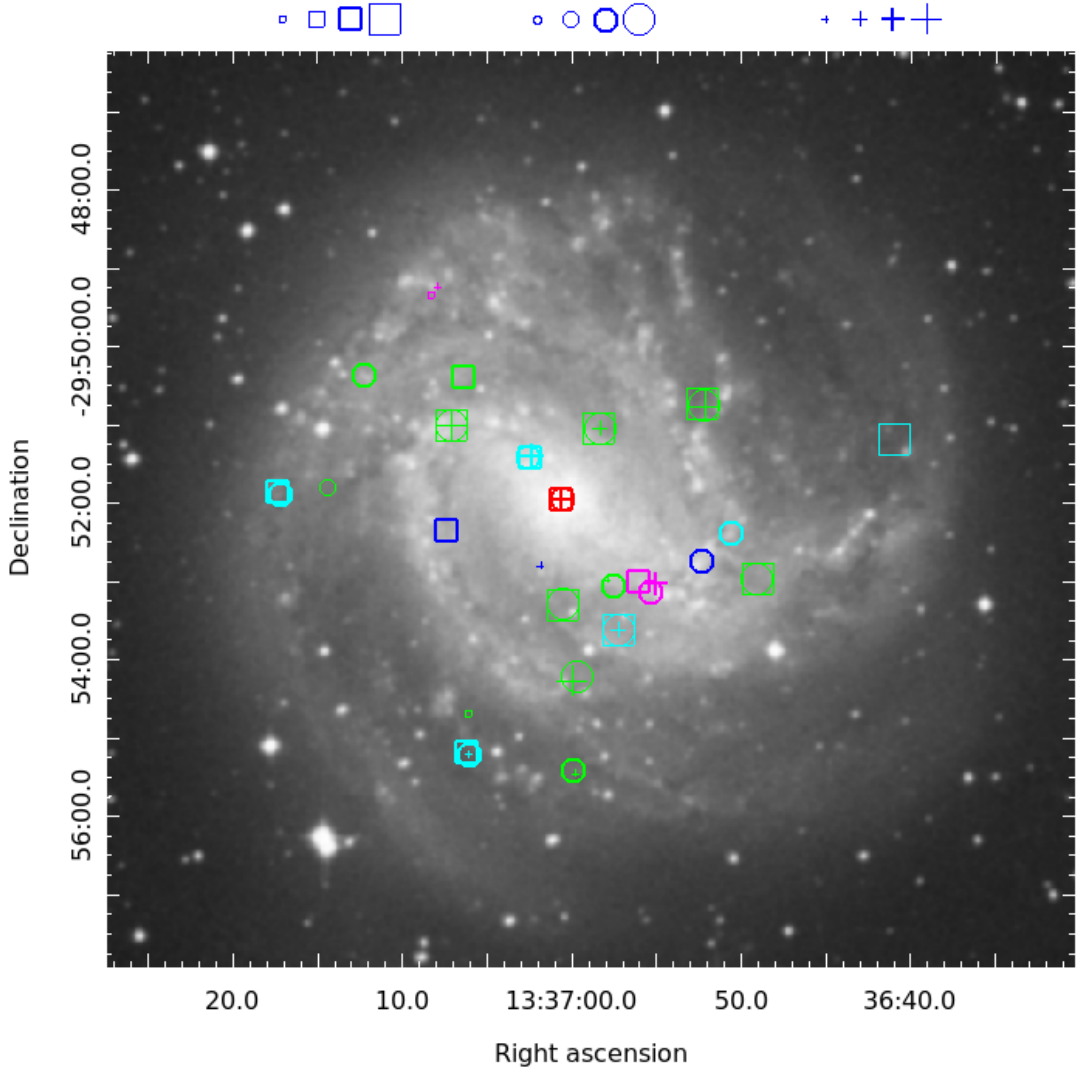
Figure 5: The source detections plotted in the same optical image of M83 as in Figure 4. The different colors denote the waveband, in which the counterpart was observed. Green: *optical_s2* (chosen based on [S II] to Hα ratio), blue: *optical* (chosen based either on [S II] or [O III] to Hα ratio), cyan: *optical_s2, radio*, magenta: *optical, radio*. The red color marks sources in the nuclear region.
The different symbols show by which camera the source was detected (box: MOS1, circle: MOS2, cross: PN). The four different sizes correspond to different hardness ratios. Smallest regions: both HRs are negative, second smallest: HR_1 is negative and HR_2 is positive, second biggest regions: HR_1 is positive and HR_2 is negative and biggest regions: both HRs are positive. See the legend above the plot for the size comparison. Second biggest regions also have greater line widths (type Ia SNR candidates).

X-ray source in CX216, corresponding to the remnants of the supernova SN1968L [12]. The remnants of SN1950B were only detected in radio (R20-064) and the `xmmsas` source detection also showed no matches in X-ray at the position of the supernova. The other two remaining historical supernovae, for which no remnants show up in my catalogue, also do not match with any detected source.

It is unexpected that only a few of the optical supernova remnant candiates from my catalogue seem to have a counterpart in X-ray detections by XMM (from the observation with the ID *0761620101*), although a significant number of the optical SNRs in my catalogue *do* have an X-ray counterpart. One possible explanation could be, that those counterparts were mostly detected with Chandra by Long et al., which has a much higher spatial resolution (0.5″) [7] and can resolve smaller sources. However, XMM is more sensitive and can detect fainter or less bright objects.

6.3. Hardness ratios

The hardness ratio HR_i of the energy band i is defined as

$$\mathrm{HR}_i = \frac{X_{i+1} - X_i}{X_{i+1} + X_i},\tag{1}$$

with the number of counts X_i in the band i [9]. This also means, that there is no hardness ratio HR_n with n being the total number of given energy bands because there is no further band to compare the n-th band to. So, considering my analysis, there are only two hardness ratios, HR_1 and HR_2, since I only look at three different energy bands (as a reminder: 0.3 eV - 0.7 eV, 0.7 eV - 1.1 eV and 1.1 eV - 4.2 eV). The errors of the hardness ratios were calcualted during the analysis with `xmmsas`. It is worth mentioning here, that the file containing all the data of the detected sources consists of four different entry lines for each one of these detections. Three of them belong to the first, the second and the third energy band, respectively, but do not contain any information on the hardness ratios. These are collected in the fourth entry line, which also provides an overview about the entire energy range of 0.3 keV up to 4.2 keV.

If the number of counts in the energy band i is smaller than the one in the energy band $i + 1$, the hardness ratio HR_i is positive. Negative hardness ratios correspond to sources with smaller numbers of counts in the higher energy band than in the lower energy band.

6.3.1. Type Ia SNR candidates

Looking back at Figure 5, the regions are of different sizes. The smallest regions are sources with both negative HR_1 and negative HR_2, whereas HR_1 is negative and HR_2 is positive for the second smallest regions. The sources of interest for the following paragraphs are the ones with positive HR_1 and negative HR_2 (second biggest regions), which is why they additionally have greater line widths for better visibility. The biggest

regions are the hardest and thus both HRs are positive. The different sizes are depicted above the plot in Figure 5. Note here, that these regions, their color and their size are completely irrelevant for the analysis. They are just presented to get an impression of the region sizes.

The reason why the hardness ratios were included in Figure 5 is that they can already reveal some information about the type of the supernova that preceded the supernova remnant. As stated earlier, the middle band is expected to contain iron L-shell line emission. Therefore, sources with highest emission in this band show signs of supernovae of type Ia (thermonuclear) such as the two remnants in Kavanagh et al. In that paper, the Fe L-shell emission can also be seen in Figure 6. Highest emission in the middle band means positive HR_1 and negative HR_2 in accordance with the general theoretical properties of the hardness ratio from Equation 1 mentioned above.

Even though the detected sources mostly have positive HR_1, the hardness ratios HR_2 are more variable and thus not all sources are good type Ia SNR candidates, but probably candidates for other types, such as the core-collapse supernovae. The positive HR_1 are however mostly the case for the two MOS cameras, whereas HR_1 is quite broadly distributed around 0 for the PN camera (see also Figure 7). Hence, the high count values in the middle band could also be a consequence of the properties of the MOS cameras, which are sometimes expected to have quite low sensitivity below $0.5\,\mathrm{keV}$. Nonetheless, the MOS cameras have the higher spectral resolution and it is still of interest to further investigate the candidates for remnants of thermonuclear supernovae.

I want to make another remark on the differences between the HRs of the different CCDs. Three sources show highest emission in the middle band for the MOS2 camera, but the PN camera did not detect this, see Figure 5. Compare also with Table 6 for this fact, where "PN" in the row of those three specific sources is written in parentheses. But as mentioned before, MOS cameras have higher spectral resolution, thus I analyze the hardness ratios based mainly on their collected data.

To do this, coordinates for sources with positive HR_1 and negative HR_2 are extracted and collected in the second column of Table 5. The positions and IDs of all sources except the last two correspond to the MOS2 CCD. The coordinates for the other cameras (if detected, see Table 6) were not included, because of positional coincidences with the MOS2 detection. The last two sources (M1X066 and M1X060) were however only detected with MOS1, so the MOS1 coordinates and IDs are given. The source IDs of the XMM sources are found in the first column. The hardness ratios HR_1 and HR_2 together with their respective uncertainties (calculated with `xmmsas`) are listed in the third column. Note here, that I include the source in the nuclear region (M2X002) for the sake of completeness in this and the next table, but I will neglect it for the analysis, because the measured data can easily be misinterpreted due to the emission from the confused nuclear region.

Williams et al. not only published a list of optical SNR candidates, but also derived zero age main-sequence (ZAMS) masses and hereby estimated progenitor masses for their

objects based on the age of the star population surrounding the object [26]. The masses are listed in the third column of Table 6 for the selected sources (Table 5) with their lower and upper boundary together with the respective Williams et al. ID of the counterpart.

Table 6 also includes the source ID in the first column as well as the B12 name of the counterpart in the second column. XMM sources M2X051 and M2X087 have two counterparts in the optical, both listed in the table. The fourth column describes by which CCD the sources were detected. If PN is written in parentheses, this highlights the differences between the hardness ratios of MOS and PN discussed above. The wavebands in which counterparts of the X-ray sources were observed, are collected in the last column.

Sources in Table 6 are all candidates for SNRs of type Ia supernovae. The star population surrounding the candidates would have to be rather old to satisfy the classification of the candidates as remnants of thermonuclear SNe. The initial masses of stars that evolve into white dwarfs (common starting point for thermonuclear SNe) are expected to be no greater than about $8\,M_\odot$.

Taking the lower boundary of the masses into account, M_{ZAMS} of sources M2X029 and M2X068 lie within the expected range. This would support the identification as remnants of type Ia supernovae, but only considering boundary conditions. Masses of sources M2X051, M2X117 and M2X026 lie between $8\,M_\odot$ and $9\,M_\odot$ within the lower boundary and match the expected progenitor mass quite well, even though not as good as the other two sources mentioned at first. The value of the mass alone of source M2X117 is however comparable to the masses of source M2X029 and M2X068 (without considering the lower boundary), so their progenitors seem to be quite similar. The masses for both counterparts of source M2X051 are very similar and indeed suggest the same object. Without considering the boundaries on the masses, none of the reported M_{ZAMS} suggests low mass progenitor stars, but rather stars of intermediate mass.

The reported masses of the other sources (M2X063, M2X087 and M1X066) seem to deviate further from the expected outcome and suggest high mass and young progenitor stars. Hence, the candidates are less likely to be remnants of type Ia SNe. However, it also seems that the higher the estimated progenitor mass, the higher the lower (and upper) boundary, so it is difficult to identify those sources based on their mass.

For the remaining sources, no masses were calculated, because there was no star formation within the last $50\,\mathrm{Myr}$ surrounding the source, so the star population is expected to be old to begin with. Williams et al. assume these are remnants of thermocuclear supernovae or runaway massive stars, the first of which would support the classification of the sources as remnants of type Ia SNe, but it was not possible to confirm this for the candidates from Table 5 and Table 6. Nevertheless, source M2X110, M2X099 and M1X060 are good candidates for remnants of low mass stars and thus good type Ia SNR candidates.

In general, Williams et al. reported 21 progenitor stars with masses below $8\,M_\odot$ and 38 sources without any masses of 237 sources in total. This suggests that only about $25\,\%$ of all sources are good type Ia SNR candidates and furthermore that the star population in M83 is rather young than old.

Table 5: The IDs and coordinates of the detections by XMM, that show highest emission in the middle band as well as hardness ratios with uncertainties.

MOS ID	RA (h,min,s)			DEC (h,$'$,$''$)			HR$_1$	ΔHR$_1$	HR$_2$	ΔHR$_2$
M2X110	13	37	12.19	-29	50	23.10	0.46	0.23	-0.73	0.24
M2X063	13	36	50.59	-29	52	24.22	0.30	0.20	-0.59	0.23
M2X029	13	36	52.31	-29	52	45.23	0.17	0.08	-0.94	0.10
M2X099	13	36	59.91	-29	55	25.98	0.23	0.27	-0.40	0.28
M2X051	13	36	55.31	-29	53	9.31	0.10	0.12	-0.97	0.13
M2X087	13	37	17.12	-29	51	53.79	0.21	0.19	-0.08	0.18
M2X117	13	37	5.97	-29	55	13.95	0.66	0.29	-0.68	0.31
M2X026	13	37	2.52	-29	51	25.58	0.68	0.18	-0.91	0.17
M2X068	13	36	57.49	-29	53	4.35	0.72	0.27	-0.61	0.23
M2X002	13	37	0.53	-29	51	58.15	0.44	0.01	-0.09	0.01
M1X066	13	37	6.28	-29	50	24.63	0.79	0.23	-1.00	0.09
M1X060	13	37	7.29	-29	52	22.49	1.00	0.28	-1.00	0.31

Table 6: The IDs of the same detected sources as in Table 5, the B12 name and the ID from Williams et al. [26] of the optical counterpart, the estimated progenitor mass in units of $M_\odot$ taken from [26], CCDs and counterparts.

MOS ID	B12 name	ID [26]	M_{ZAMS}	CCDs	counterparts
M2X110	B12-210	288	-	MOS2	optical
M2X063	B12-048	053	$18.4^{+0.30}_{-6.70}$	MOS2	optical, radio
M2X029	B12-060	070	$8.02^{+2.28}_{-0.32}$	MOS2	optical
M2X099	B12-127	153	-	MOS2, (PN)	optical
M2X051	B12-089	104	$11.26^{+1.24}_{-2.66}$	MOS1, MOS2, PN	optical, radio
	B12-091	106	$10.64^{+1.06}_{-2.54}$		
M2X087	B12-221	302	$30.31^{+4.39}_{-16.91}$	MOS2, MOS1	optical, radio
	B12-223	304	$38.24^{+3.76}_{-26.54}$		
M2X117	B12-169	231	$8.35^{+5.05}_{-0.25}$	MOS2, MOS1, (PN)	optical, radio
M2X026	B12-150	203	$11.45^{+7.25}_{-2.85}$	MOS2, MOS1, PN	optical, radio
M2X068	B12-115	130	$8.38^{+4.12}_{-1.08}$	MOS2, (PN)	optical
M2X002	-	-	-	MOS2, MOS1, PN	nuclear
M1X066	B12-171	234	$26.60^{+2.60}_{-15.70}$	MOS1	optical
M1X060	B12-182	250	-	MOS1	optical
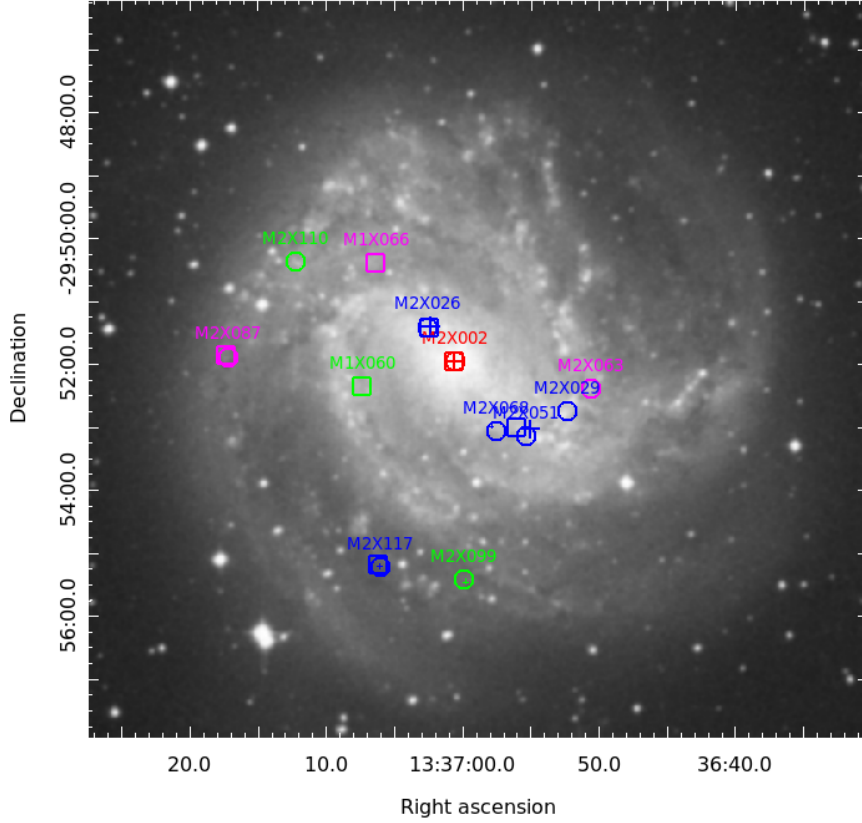
Figure 6: The type Ia SNR candidates from Table 5. The colors do not represent the wavebands from the counterparts, but the progenitor mass. The red region is the source in the nuclear region. Green regions are low mass stars, blue regions are intermediate mass stars and magenta sources are high mass stars. The different symbols of the regions correspond to the CCD by which the sources were detected, the same way as in Figure 5.

Figure 6 presents only those sources from Figure 5, that are type Ia SNR candidates. The colors in the figure represent the above estimated progenitor mass. Green regions correspond to low mass stars, blue regions to stars of intermediate mass and magenta regions to high mass stars. The red region is the source in the nuclear region for which no mass was given. Stars of either mass do not seem to be found preferably in the inner or the outer regions of M83.

The sources that show masses below $8\,M_\odot$ within the lower boundary (M2X029 and M2X068) only have optical counterparts. Sources without reported masses (and thus remnants in considerably older star populations) also show only optical counterparts. It may be concluded from this that remnants of type Ia SNe tend to not having radio counterparts. However, sources M2X051, M2X117 and M2X026 do not deviate far beyond $8\,M_\odot$ within the lower boundary and additionally have radio counterparts. Plus, as

mentioned above, without considering the lower boundary of the masses, the progenitor of source M2X117 seems to be similar to the ones of source M2X029 and M2X068. Furthermore, source M1X066, which showed a far bigger mass, has only an optical counterpart. The last three facts suggest, no statement should be made about the wavebands of the counterparts of type Ia SNR candidates.

6.3.2. Hardness ratio diagrams

After having classified the sources detected by XMM, I also plotted hardness ratio diagrams for each of the EPIC instruments. Note here, that because of the classification, I ignored sources without counterparts in my catalogue. That is the reason why the following plots do not contain all detected sources. In Figure 7, HR_2 is plotted in respect to HR_1 for MOS1 (upper left), MOS2 (upper right) and PN (lower left).

All three cameras detected many counts originating from the nuclear region of the galaxy (red "x" in all plots respectively). This results in very low uncertainty of the two hardness ratios, which seems favorable at first sight. But, due to lots of confused emission, it is difficult to analyze the spectral properties of the source in the nuclear region. Since the nuclear region is very bright compared to other sources, the CCD arrays do not have to
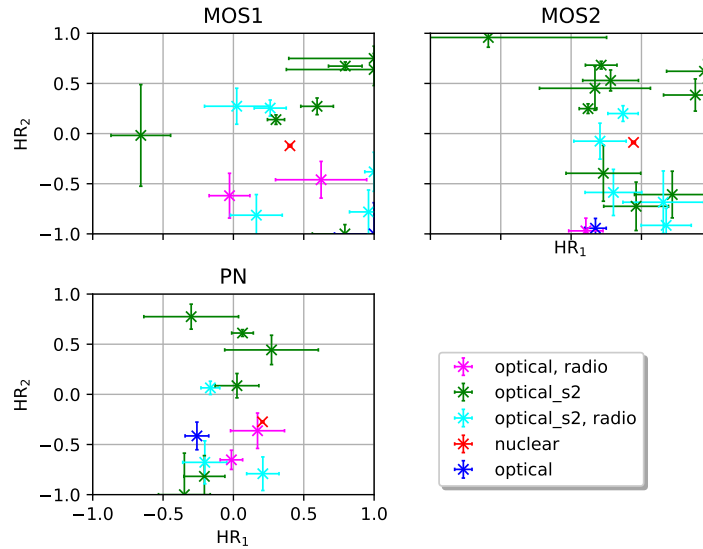
Figure 7: The hardness ratio diagram for each camera. HR_2 was plotted over HR_1. The red cross denotes the source in the confused nuclear region for all three cameras. The other colors correspond to the coloring in Figure 5, though the symbol of the sources are always crosses, since the differentiation between the cameras is achieved by three separate plots. The errors for both hardness ratios were calculated by `xmmsas` during the data processing.

be that sensitive to detections and a high and similar count number in all energy bands and for all cameras is expected. Hence, according to Equation 1, both HRs should yield values around 0. This expected outcome can be observed in the three hardness ratio plots, where the red "x" denoting the nuclear region is close to zero for both HRs, with minor deviations.

The MOS cameras have a high spectral resolution, so looking at their plots could already reveal some information on spectral properties of the SNRs. Indeed, this seems to be the case. As argued earlier, oxygen emission lines are prominent in the softest band. But most of the sources were chosen because of prominent [S II] to Hα emission ratio. So, higher count numbers in the two harder energy bands are expected. This can be seen in the MOS2 plot, where only one source with an optical counterpart has a negative HR_1. This also holds for MOS1, except here one additional source with a radio counterpart deviates from this interpretation.

HR_2 tends to be negative for most sources, that have a reported radio counterpart in my catalogue, marked in cyan and magenta in the plots, whereas sources that only have optical counterparts ([S II] or either [S II] or [O III]) seem to have a positive HR_2. However, this is not the case for all sources and some of them differ from this interpretation, especially the sources with only optical counterparts in the PN plot. Four have positive HR_2 and three have negative HR_2, so it is difficult to analyze the HRs from this point of view.

The hardness ratios can also be compared to those reported in [9, p. 7]. However, it has to be taken into account that the energy bands therein were chosen differently. Ducci et al. defined five bands opposed to the three bands used within this project. The first ranging from $0.2\,keV$ to $0.5\,keV$, the second from $0.5\,keV$ to $1\,keV$ and the third from $1\,keV$ to $2\,keV$. The last two bands cover an energy range of $2\,keV$ up to $4.5\,keV$ and $4.5\,keV$ up to $12\,keV$ [9].

In the upper plot of Figure 3 in Ducci et al., one supernova remnant is denoted as the orange diamond. It has a HR_1 of approximately 0 and its HR_2 is around 0.5. Even though the bands in the paper were chosen differently, band 1 and 2 are similar to mine. The HR_1 of the two MOS cameras are mostly all positive, but are not all located around $HR_1 = 0$, as in the plot in [9] and seem to drift to the upper boundary of $HR_1 = 1$. Since the PN camera is the most sensitive out of the three, statistically more reliable data measured by this CCD array might be expected. The hardness ratios HR_1 of the PN camera all lie between -0.5 and 0.5, which matches only a little bit better the HR_1 of the Ducci et al. paper. However, the assumption that HR_1 should measure approximately zero for all the supernova remnants, is based only on one single source in the upper plot of Figure 3 in [9] and it is not justified to constrain HR_1 to one specific value based on one single source in Ducci et al. Moreover, not all sources should show the same value of HR_1, unless they are all the remnants of the same type of SN, which is not to be expected. Therefore, the comparison between my hardness ratio diagram and the one from Ducci et al. can only give a rough impression of the HRs of supernova remnants, but cannot reveal more precise information.

HR_2 of around 0.5 cannot be reproduced well by my data sets for any of the cameras (in the sense that they do not crowd around 0.5). Instead, the hardness ratios HR_2 vary between the lower and upper boundary of -1 and 1, respectively. But again, the Ducci et al. paper only reported one single SNR, so it is difficult to constrain the HR_2 to one single value. The broad distribution of HR_2 in my three plots suggests rather large variability in the physical (especially spectral) properties of the SNRs and may also be a hint at differences (type Ia SN or core-collapse SN) between the different remnants.

Core-collapse SNe are expected to have emission with energies higher than $1.1\,keV$, so HR_2 would be positive. The plots show that about half of the sources have positive HR_2 and thus show characteristics of harder sources. It could also be differentiated between younger and older SNRs. Harder sources are believed to often be young SNRs (non-thermal, young, hot plasma), although this does not automatically allow to differentiate between type Ia remnants or core-collapse SNRs.

In the middle and lower plot of Figure 3 in [9], the hardness ratio of the supernova remnant decreases with increasing energy. This suggests a softer source and indeed SNRs are expected to be emitters of softer X-rays compared to other X-ray emitters such as active galactic nuclei or pulsar wind nebulae.

6.4. Counts and count rates

In addition to the hardness ratios, I also plotted the counts and the count rates as a measure for the brightness of a source in Figure 8 and Figure 9, respectively. The uncertainties were once again calculated with `xmmsas`. The counts and count rates for the source lying in the nuclear region were ignored during the development of the plot, since much higher values are expected compared to the other sources outside the nuclear region. It would be difficult to distinguish those other sources from one another and interpret the counts as well as count rates because the scaling would crowd the plot in their count range. By neglecting the nuclear region, the x-axis scales differently, so the disucussion can be conducted properly. Later on, the spectrum of two XMM sources with high count numbers will be examined. The source in the nuclear region would fall in the category of high count numbers. However, it is reasonable to ignore it in either discussion, since the values of rates and counts are not very reliable.

The similarities between the count plot and the count rate plot are clearly visible, as expected. The counts of each detection are essentially rescaled by the exposure time. This time is not exactly the same for every detection but very similar. The only greater deviation between the number of counts and the count rate can be seen for the right of both magenta sources in the PN plot. This suggests a larger deviation in the exposure time compared to all other sources. Since the exposure times are an essential attribute in the entry lines of the detected sources, this suggests a systematic error (or at least some systematical problems, such as handling of the telescope or constructional difficulties). I would also not rule out compromised pixels as source of error, since it cannot be certainly
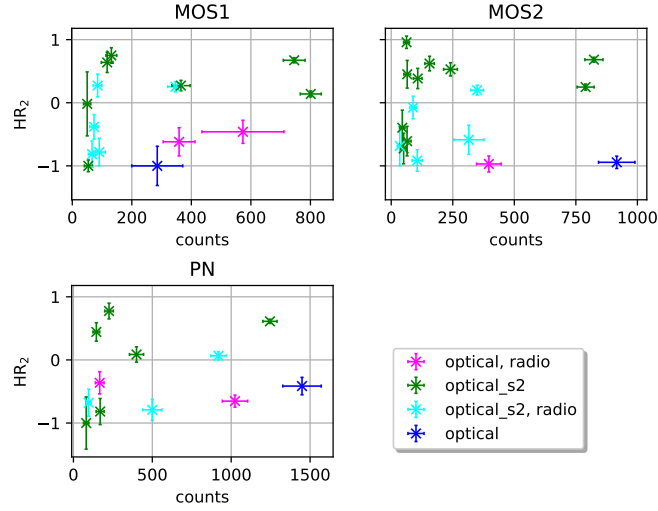
Figure 8: The total number of counts for each of the detectors. The different colors denote once more which type of counterpart belongs to the given XMM source. The emission coming from the nuclear region was neglected in the creation of this plot, since a much higher count number is expected due to its brightness and diffuse emission, compared to the other detections.
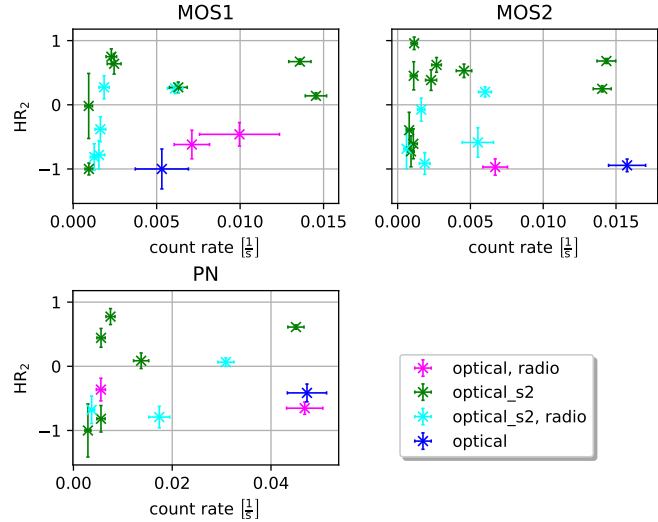
Figure 9: The total number of count rates for each of the detectors. The different colors denote once more which type of counterpart belongs to the given XMM source. The emission coming from the nuclear region was neglected in the creation of this plot, since a much higher count number (also count rate number, when assuming similar exposure times) is expected due to its brightness and diffuse emission, compared to the other detections.

said that the exposure time is wrong. Instead, the count value could be wrong to begin with.

Out of all three detectors, PN is the most sensitive one, resulting in the conceptionally and naturally higher counts and count rates.

6.5. Spectra

Evaluating the count (and also count rate) plots, I decided to further examine two sources with many counts, since they are very bright. This makes the analysis of the spectrum more reliable. Remember here, that I neglected the source in the nuclear region for this discussion.

Furthermore, at this point of the analysis, the previously addressed difficulties concerning the correlations of XMM sources with objects in my catalogue first arised. The difficulties were a follow-up of classifying entries in my catalogue as counterparts of detected sources, that lie within a $12''$ radius surrounding the source. Four sources were initially chosen for the discussion of the spectrum, as they were the brightest ones according to the initial plots in Figure 8. Looking at the extracted spectra and cross-correlating the coordinates of the XMM source with previous work on M83, showed that two of the four sources are actually ultraluminous X-ray (ULX) sources [9, 21], which explains their high number of counts compared to other detections. The two remaining sources are most likely also ULX or objects with similar properties (generally very bright in X-rays). This had an immediate effect on the comparison of XMM sources with my catalogue, since I allowed too great positional errors on the counterparts and especially ULX would outshine the very near supernova remnant candidate from my catalogue. As a consequence, I had to drop the counterparts in and close to the R_{12} circle and delete the hardness ratios as well as counts and count rates from the corresponding sources from the plots. The spectra from the remaining point-like sources (that now solely have counterparts that lie within a $6''$ radius) were extracted using analysis tools from `xmmsas` [16] once again (see subsection B.5 for specific commands).

After the re-evaluation, I chose to extract the spectrum from the objects named A and B from this point forward, listed in Table 7. The table includes the IDs of the sources from all three detectors in the second column and their respective coordinates in the third column (to make plausible here, that it is arguably the same object detected by each camera). The corresponding counts are given in column four as well as the name of the optical counterpart(s) in my catalogue in the fifth column. Note here, that source A has two optical counterparts. To avoid confusion, I shall also note that it was not distinguished between the detectors for the counterpart(s). The counterparts belong to all three detectors equally for the respective source. I shall also note, that neither source A, nor source B is the source with the probably incorrect exposure time.

It is important to mention, that the source A is featured in both the Williams et al. paper as well as the Long et al. paper. Williams et al. described the source as 'optical imaging

Table 7: The XMM IDs, coordinates, counts and the name of the optical counterpart (optical c.) of two objects (A and B). Note that the object A has two counterparts in my catalogue. To avoid confusion, also note that I did not distinguish between detectors for the counterpart(s). The counterpart(s) correspond(s) to all three CCDs equally for the respective source.

	XMM ID	RA (h,min,s)			DEC (h,$'$,$''$)			counts	optical c.
A	M1X009	13	37	07.02	−29	51	00.83	745.38 ± 36.57	D10-1-02
	M2X007	13	37	07.01	−29	51	00.80	823.37 ± 36.74	B12-179
	PNX008	13	37	07.06	−29	51	00.82	1245.60 ± 45.10	
B	M1X016	13	36	57.20	−29	53	38.11	346.43 ± 25.98	B12-112
	M2X013	13	36	57.23	−29	53	38.61	349.11 ± 25.66	
	PNX021	13	36	57.18	−29	53	37.61	919.00 ± 48.90	

candidate strongly confirmed by optical spectroscopy (e.g. spectroscopic [S II]:H$\alpha > 0.5$)' [26, p. 2], whereas Long et al. suggested it is likely a black hole X-ray binary (BH XRB), despite the positional coincidence with B12-179 [12]. Source B is classified the same way as source A in Williams et al. and additionally identified as XRB in Ducci et al. Hence, both sources were seen as probable SNR candidates in the optical, but rather as XRBs in X-rays. This suggests that the two sources might be supernova remnants with either a neutron star or a black hole in the center. The exact composition of the astronomical object shall not be the major focus of this discussion. I rather want to concentrate the discussion on the analysis of the two extracted spectra, based on the assumption that they indeed are supernova remnants, as assumed in Williams et al.

The spectra for both sources were fitted according to an APEC model for thermal plasma as well as a powerlaw in `xspec` (APEC+powerlaw model). The fit parameters can be seen in Table 8 and Table 9. The fit parameters for both sources suggest that the spectrum is mostly thermal. In particular, the photon index γ suggests that the probability, the emission of the examined sources comes from non-thermal electron distributions is low. If the photon index would lie between 1 and 2, the spectrum is expected to belong to objects such as AGNs or pulsar wind nebulae. These objects would generally show much harder X-rays and thus increasing hardness ratios for increasing energy band number. SNRs are expected to be softer X-ray emitters and their hardness ratios would decrease with increasing band number (after reaching its maximum in the band, where most counts were detected). This can be observed in the HR plots in Figure 3 in Ducci et al., where the one classified SNR peaks in the hardness ratio HR_2 ($HR_2 \approx 0.5$) and decreases in the two plots below ($HR_4 \approx -0.3$). Powerlaw fits yielded photon indices 2.601 ± 0.130 and 2.153 ± 0.289 for source A and B respectively, which hints at a rather thermal than non-thermal as well as a generally softer spectrum, supporting the identification of the two sources as SNRs. Compared to source B, source A seems to be harder, suggesting harder X-rays emitted by an additional component in the object besides the SNR. This additional component could be a pulsar and/or a pulsar wind nebula.

For both sources, the fit routine of `xspec` also yielded 90 % confidence intervals to constrain the value range of the fitted parameter. This was however not possible for the norm of the thermal component of the respective source, because of their high uncertainties. The thermal component of source B did not yield a statistically acceptable confidence interval as well, since the relative uncertainty is high compared for example to the thermal component of source A.

Since it was argued that the probability, the spectrum consists of rather two thermal components, was considered higher, an APEC+APEC model was also fitted to both spectra in addition to the APEC+powerlaw model. The resulting fit parameters for source A and B can be seen in Table 10 and Table 11, respectively. The respective norms of component 1 and the first thermal component of source B did again not result in a reliable confidence interval.

Both models show that fits for source A yield more precise values than for source B. One possible explanation could be that source B has lower detected counts for each CCD, thus the fits are based on fewer data and ultimately not as good as for source A.

The results of the plotting and fitting of the spectra according to the APEC+powerlaw model are shown in two double-logarithmic plots in Figure 10 and Figure 11 for source A and B, respectively. In both plots, the black solid lines are MOS1 data, red solid lines are MOS2 data and the green solid lines are PN data. Because of higher sensitivity of the PN camera, the green data show higher count values.

As stated in subsection 3.1, Kavanagh et al. did research on supernova remnants in the LMC and extracted the spectrum of two SNRs shown in their Figure 9. They based their discussion only on the PN spectrum, so I will later compare it only to my PN data and not the MOS data.

The Fe L-shell component of the spectrum is prominent between 0.7 keV and 1.1 keV (in the middle one of the three energy bands). Therefore, if the spectrum mainly consists of this iron emission line, high X-ray emission in this energy range should be found, which could look like a 'Fe L-shell "bump"' [10, p. 8]. Before examining the different components of the spectrum itself, I shall mention that the sources A and B in my detections are not as bright as the two sources reported in Figure 9 in Kavanagh et al. – *MCSNR J0506-7025* and *MCSNR J0527-7104* – and have a much flatter spectrum than Kavanagh et al. sources. Another clearly recognizable difference is that the X-ray emission decreases far more rapidly beyond 1 keV in the spectrum of the two Kavanagh et al. sources (adding to the impression of the flatness of the spectrum of my two investigated sources). In principle, source A and B have quite similar spectra, when it comes to the general distribution of the brightness over energy, suggesting similar objects.

As far as the Fe L-shell bump is concerned, sources A and B do not have comparably significant emission as the two sources in the work of Kavanagh et al. The spectrum seems to peak only beyond 1.1 keV (even beyond 1.5 keV for source A), suggesting other dominant (harder) components, such as neon, magnesium, silicon or sulphur, although no distinctive emission line can be seen in the spectrum. Strong emission in harder

Table 8: Fit parameters from the APEC+powerlaw model for source A.

parameter	value	90 % confidence interval
galactic nH in cm^{-2}	$(1.674 \pm 0.162) \times 10^{22}$	$1.410 < \mathrm{nH} < 1.970$
$k_\mathrm{B}T$ in keV	$(5.523 \pm 0.466) \times 10^{-2}$	$0.047 < k_\mathrm{B}T < 0.083$
norm in cm^{-5}	119.429 ± 212.979	-
γ	2.601 ± 0.130	$2.400 < \gamma < 2.820$
norm in $\mathrm{photons\,keV}^{-1}\,\mathrm{cm}^{-2}\,\mathrm{s}^{-1}$ at 1 keV	$(1.615 \pm 0.298) \times 10^{-4}$	$12 \times 10^{-5} < \mathrm{norm} < 22 \times 10^{-5}$

Table 9: Fit parameters from the APEC+powerlaw model for source B.

parameter	value	90 % confidence interval
galactic nH in cm^{-2}	$(0.313 \pm 0.173) \times 10^{22}$	$0.150 < \mathrm{nH} < 0.730$
$k_\mathrm{B}T$ in keV	$(3.211 \pm 1.712) \times 10^{-2}$	-
norm in cm^{-5}	3.066 ± 19.426	-
γ	2.153 ± 0.289	$1.730 < \gamma < 2.720$
norm in $\mathrm{photons\,keV}^{-1}\,\mathrm{cm}^{-2}\,\mathrm{s}^{-1}$ at 1 keV	$(1.509 \pm 0.514) \times 10^{-5}$	$9.1 \times 10^{-6} < \mathrm{norm} < 28.3 \times 10^{-6}$

Table 10: Fit parameters from the APEC+APEC model for source A.

parameter	value	90 % confidence interval
galactic nH in cm^{-2}	$(1.438 \pm 0.114) \times 10^{22}$	$1.264 < \mathrm{nH} < 1.628$
$k_\mathrm{B}T_1$ in keV	$(5.807 \pm 0.494) \times 10^{-2}$	$0.049 < k_\mathrm{B}T_1 < 0.077$
norm 1 in cm^{-5}	20.471 ± 30.580	-
$k_\mathrm{B}T_2$ in keV	2.689 ± 0.198	$2.403 < k_\mathrm{B}T_2 < 3.033$
norm 2 in cm^{-5}	$(2.401 \pm 0.203) \times 10^{-4}$	$21 \times 10^{-5} < \mathrm{norm} < 28 \times 10^{-5}$

Table 11: Fit parameters from the APEC+APEC model for source B.

parameter	value	90 % confidence interval
galactic nH in cm^{-2}	$(0.258 \pm 0.154) \times 10^{22}$	$0.067 < \mathrm{nH} < 0.610$
$k_\mathrm{B}T_1$ in keV	$(3.072 \pm 1.549) \times 10^{-2}$	-
norm 1 in cm^{-5}	1.412 ± 9.816	-
$k_\mathrm{B}T_2$ in keV	4.154 ± 1.277	$2.548 < k_\mathrm{B}T_2 < 7.580$
norm 2 in cm^{-5}	$(3.147 \pm 0.555) \times 10^{-5}$	$23.9 \times 10^{-6} < \mathrm{norm} < 44 \times 10^{-6}$

components hint at core-collapse supernovae and thus remnants of stars in younger populations, rather than thermonuclear (type Ia) supernovae and therefore probably SNRs of older stars, as mentioned in subsubsection 6.3.1. Harder components are consistent with the onion-like shell structure of stars that go through the core-collapse process and are expected to have ejecta rich of elements heavier than carbon and oxygen. The fusion of heavier elements is possible because the initial mass of stars ending in core-collapse SNe is higher compared to the ones ending in white dwarfs.

In subsubsection 6.3.1, candidates for remnants of type Ia SNe were presented (chosen because of highest emission in the middle band). Source A and B are not featured in the list of these candidates, also suggesting remnants of core-collapse SNe. The hardness ratios HR_1 and HR_2 are positive for both source A and source B. Hence, also high emission in the hardest of the three bands, where emission lines of heavier elements are expected, can be observed. The identification of source A and B as core-collapse supernova remnants would stand in contrast to the sources in Kavanagh et al., which are believed to be type Ia SNRs because of dominant iron emission in their spectrum. MCSNR J0527-7104 is furthermore believed to have clumpy ejecta and H admixed into the Fe [10]. Differences in the identification arise from the above explained deviations between the X-ray spectra in this project and the work of Kavanagh et al.
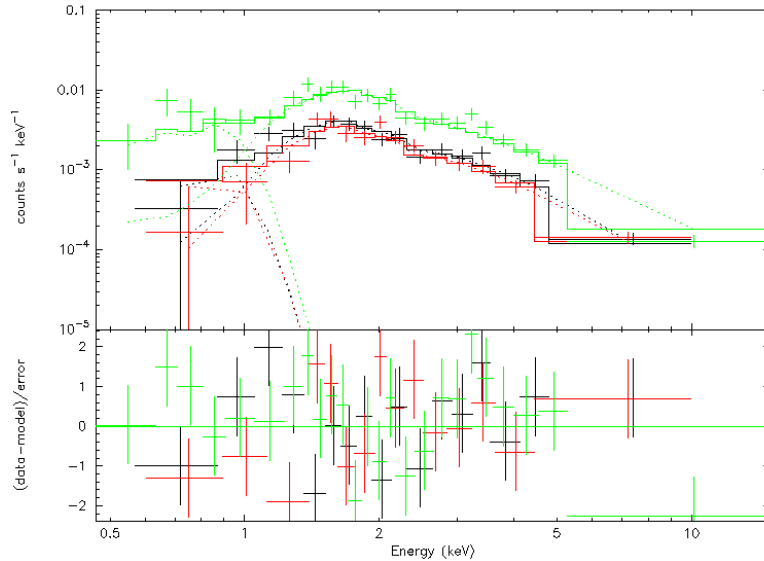
Figure 10: Double-logarithmic plot of the spectrum of source A for all three cameras and two fits per camera (fits based on the APEC+powerlaw model). Solid lines are data points and dashed lines are fits. Black color corresponds to MOS1 data, MOS2 data are red and PN data are green. The residuals of the fits are at the bottom of the plot with the same coloring.
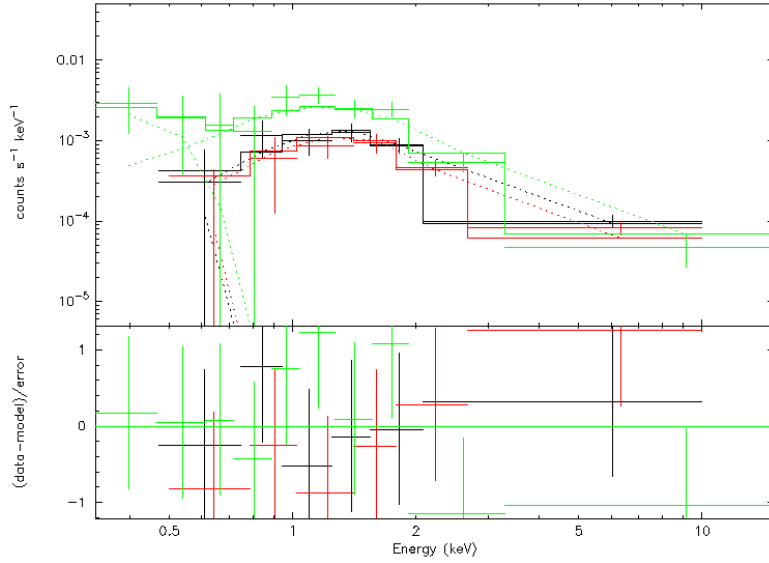
Figure 11: Double-logarithmic plot of the spectrum of source B for all three cameras and two fits per camera (fits based on the APEC+powerlaw model). Solid lines are data points and dashed lines are fits. Black color corresponds to MOS1 data, MOS2 data are red and PN data are green. The residuals of the fits are at the bottom of the plot with the same coloring.

7. Summary and Outlook

M83 is an intermediate spiral galaxy with active star forming regions in the spiral arms. Those spiral arms are clearly discernible in optical images of the galaxy, due to its nearly face-on characteristic. M83 hosted six to seven historical supernovae within the last century, of which four have optical supernova remnant counterparts. Of those four, three SNRs were also reported in X-rays and three in radio. One SN only has a radio counterpart and two have not yet revealed any remnants up to this point.

By consulting and cross-correlating previously published catalogues of astronomical objects in the M83 galaxy, I could develop my own catalogue of supernova remnant candidates. This catalogue contains the coordinates of optical SNRs and supernova remnant candidates as well as possible counterparts in other wavebands (X-rays and/or radio). Plotting the supernova remnant candidates in optical images of M83 revealed their position and thus the coordinates of their progenitor star (if the source really is a SNR) within the galaxy. As expected, the sources mostly lie within the spiral arm structure of the galaxy and can even be found in the outmost regions of M83.

Supernova remnants are known for their strong X-ray emission. Therefore, the analysis of sources in M83 was based on X-ray observations by the XMM-Newton telescopes (consisting of three different CCD arrays: MOS1, MOS2 and PN). The data acquired by

XMM was processed using XMM analysis tools and resulting 359 detected sources were compared with my catalogue containing SNR candidates. Sources with counterparts in my catalogue are likely supernova remnants. Those sources were also plotted in images of the galaxy, which follow the spiral arm structure of M83 as well.

Hardness ratios were used to determine, in which energy band the X-ray sources show highest emission. Twelve sources show highest X-ray emission in the middle band from $0.7\,\mathrm{keV}$ to $1.1\,\mathrm{keV}$, containing the iron L-shell line. Those twelve sources were further investigated as type Ia SNR candidates, because Fe L-shell line emission is often observed in the spectrum of thermonuclear SNRs. The investigation was based on estimated progenitor masses and star formation rates surrounding the source. Objects M2X110, M2X099 and M2X002 were concluded to be specifically good type Ia SNR candidates.

The spectrum of two further sources, M2X007 and M2X013, that did not satisfy the criteria for type Ia SNR candidates, was extracted, plotted and fitted. Fit parameters suggest two thermal components, common for SNRs, rather than one thermal component and a photon (spectral) index. The hardness ratios and harder X-ray emission observed in their spectrum lead to the assumption of M2X007 and M2X013 being two core-collapse supernova remnant candidates, in addition to the three good thermonuclear SNR candidates. This differentiation between remnants of SNe of type Ia and core-collapse SNe was the main goal of this project.

However, further studies on SNRs – mainly on their spectral properties – have to be done in the future to be able to ultimately classify the X-ray sources detected by XMM-Newton in the M83 galaxy. X-ray studies could also be combined with radio and optical data, allowing analysis in a broader energy range of the electromagnetic spectrum. More precise X-ray data could play an important role in future work on X-ray properties of SNRs. Another aspect in the classification of objects could be the light curves of SNe to get an impression of their brightness on longer time scales. This requires however longer exposure times. Performing this additional analysis may serve as a crucial next step towards the classification of objects and supernova remnants in M83.

References

[1] William P. Blair, P. Frank Winkler, and Knox S. Long. "Erratum II: "The Magellan /IMACS Catalog of Optical Supernova Remnant Candidates in M83" (2012, ApJS, 203, 8; also 2013, ApJS, 207, 40)". In: *The Astrophysical Journal Supplement Series* 229.2 (Apr. 2017), p. 43. DOI: 10.3847/1538-4365/aa6683. URL: https://doi.org/10.3847/1538-4365/aa6683.

[2] William P. Blair, P. Frank Winkler, and Knox S. Long. "ERRATUM: "THE MAGELLAN/IMACS CATALOG OF OPTICAL SUPERNOVA REMNANT CANDIDATES IN M83" (2012, ApJS, 203, 8)". In: *The Astrophysical Journal Supplement Series* 207.2 (Aug. 2013), p. 40. DOI: 10.1088/0067-0049/207/2/40. URL: https://doi.org/10.1088/0067-0049/207/2/40.

[3] William P. Blair, P. Frank Winkler, and Knox S. Long. "THE MAGELLAN/IMACS CATALOG OF OPTICAL SUPERNOVA REMNANT CANDIDATES IN M83". In: *The Astrophysical Journal Supplement Series* 203.1 (Nov. 2012), p. 8. DOI: 10.1088/0067-0049/203/1/8. URL: https://doi.org/10.1088/0067-0049/203/1/8.

[4] William P. Blair et al. "AN EXPANDEDHST/WFC3 SURVEY OF M83: PROJECT OVERVIEW AND TARGETED SUPERNOVA REMNANT SEARCH". In: *The Astrophysical Journal* 788.1 (May 2014), p. 55. DOI: 10.1088/0004-637x/788/1/55. URL: https://doi.org/10.1088/0004-637x/788/1/55.

[5] B.W. Carroll and D.A. Ostlie. *An Introduction to Modern Astrophysics.* Cambridge University Press, 2017. ISBN: 9781108422161. URL: https://books.google.de/books?id=PYOwDwAAQBAJ.

[6] *Cassiopeia A, Chandra X-ray observatory.* URL: https://chandra.harvard.edu/photo/2017/casa_life/.

[7] *Chandra Specifications.* URL: https://chandra.harvard.edu/about/specs.html.

[8] Michael A. Dopita et al. "SUPERNOVA REMNANTS AND THE INTERSTELLAR MEDIUM OF M83: IMAGING AND PHOTOMETRY WITH THE WIDE FIELD CAMERA 3 ON THEHUBBLE SPACE TELESCOPE". In: 710.2 (Jan. 2010), pp. 964–978. DOI: 10.1088/0004-637x/710/2/964. URL: https://doi.org/10.1088/0004-637x/710/2/964.

[9] Ducci, L. et al. "X-ray source population study of the starburst galaxy Mwith XMM-Newton". In: *A&A* 553 (2013), A7. DOI: 10.1051/0004-6361/201321035. URL: https://doi.org/10.1051/0004-6361/201321035.

[10] P. J. Kavanagh et al. "Two evolved supernova remnants with newly identified Fe-rich cores in the Large Magellanic Cloud". In: *aap* 586, A4 (Feb. 2016), A4. DOI: 10.1051/0004-6361/201527414. arXiv: 1510.08922 [astro-ph.HE].

[11] M. König, S. Binnewies, and P. Helbig. *The Cambridge Photographic Atlas of Galaxies.* Cambridge University Press, 2017. ISBN: 9781108103091. URL: https://books.google.de/books?id=OEszDwAAQBAJ.

[12]   Knox S. Long et al. "A DEEP CHANDRA ACIS SURVEY OF M83". In: 212.2 (May 2014), p. 21. DOI: 10.1088/0067-0049/212/2/21. URL: https://doi.org/10.1088/0067-0049/212/2/21.

[13]   P. Maggi et al. "The population of X-ray supernova remnants in the Large Magellanic Cloud". In: *aap* 585, A162 (Jan. 2016), A162. DOI: 10.1051/0004-6361/201526932. arXiv: 1509.09223 [astro-ph.HE].

[14]   *NASA/IPAC Extragalactic Database*. URL: https://ned.ipac.caltech.edu/.

[15]   Thomas D. Russell et al. "A new radio catalogue for M83: supernova remnants and H ii regions". In: *Monthly Notices of the Royal Astronomical Society* 495.1 (May 2020), pp. 479–501. ISSN: 0035-8711. DOI: 10.1093/mnras/staa1177. eprint: https://academic.oup.com/mnras/article-pdf/495/1/479/34136023/staa1177.pdf. URL: https://doi.org/10.1093/mnras/staa1177.

[16]   *SAS Threads*. URL: https://www.cosmos.esa.int/web/xmm-newton/sas-threads.

[17]   Manami Sasaki. *Interstellar Medium – Lecture Notes*.

[18]   Frederick D. Seward and Philip A. Charles. *Exploring the X-ray Universe*. 2nd ed. Cambridge University Press, 2010. DOI: 10.1017/CBO9780511781513.

[19]   *SIMBAD*. URL: http://simbad.u-strasbg.fr/simbad/.

[20]   *SkyView*. URL: https://skyview.gsfc.nasa.gov/current/cgi/query.pl.

[21]   Roberto Soria et al. "THE BIRTH OF AN ULTRALUMINOUS X-RAY SOURCE IN M83". In: *The Astrophysical Journal* 750.2 (Apr. 2012), p. 152. DOI: 10.1088/0004-637x/750/2/152. URL: https://doi.org/10.1088/0004-637x/750/2/152.

[22]   *The European Photon Imaging Camera (EPIC) onboard XMM-Newton*. URL: https://www.cosmos.esa.int/web/xmm-newton/technical-details-epic.

[23]   *The Reflection Grating Spectrometer (RGS) onboard XMM-Newton*. URL: https://www.cosmos.esa.int/web/xmm-newton/technical-details-rgs.

[24]   *Tycho's SNR, Chandra X-ray observatory*. URL: https://chandra.harvard.edu/photo/2005/tycho/.

[25]   *WebPIMMS - A Mission Count Rate Simulator from NASA's HEASARC: Tools*. URL: https://heasarc.gsfc.nasa.gov/cgi-bin/Tools/w3pimms/w3pimms.pl.

[26]   Benjamin F. Williams et al. "The Masses of Supernova Remnant Progenitors in M83". In: *The Astrophysical Journal* 881.1 (Aug. 2019), p. 54. DOI: 10.3847/1538-4357/ab2190. URL: https://doi.org/10.3847/1538-4357/ab2190.

[27]   P. Frank Winkler, William P. Blair, and Knox S. Long. "A Spectroscopic Study of the Rich Supernova Remnant Population in M83". In: 839.2 (Apr. 2017), p. 83. DOI: 10.3847/1538-4357/aa683d. URL: https://doi.org/10.3847/1538-4357/aa683d.

[28]   *XMM-Newton Science Archive Search*. URL: http://nxsa.esac.esa.int/nxsa-web/#search.

A. Catalogue

Table 12.1 to Table 12.7 contain the entire supernova remnant catalogue including all 299 optical references and their counterparts in other wavebands. The first part of the SNR catalogue was previously shown as an example in Table 3 in subsection 4.5.

Table 12.1: SNR catalogue with optical references and coordinates, X-ray counterparts and coordinates, radio counterparts and coordinates as well as the informative flag column.

optical	RA (h,min,s)	DEC (h,′,′′)	X-ray	RA (h,min,s)	DEC (h,′,′′)	radio	RA (h,min,s)	DEC (h,′,′′)	flags[b]
B12-001	13 36 39.99	−29 51 35.10	X055	13 36 40.73	−29 51 9.10				s2
B12-002	13 36 40.35	−29 51 6.52	CX019 (M1X047)	13 36 40.87	−29 51 17.80				s2
B12-003	13 36 40.90	−29 51 17.71				R20-008	13 36 40.90	−29 51 17.80	
B12-004	13 36 41.50	−29 52 15.89							s2
B12-005	13 36 41.58	−29 49 56.32							
B12-006	13 36 42.33	−29 52 17.40							
B12-007	13 36 42.72	−29 52 35.00				R20-015	13 36 42.73	−29 52 35.40	
B12-008	13 36 43.70	−29 50 45.89							s2
B12-009	13 36 43.82	−29 52 11.21							
B12-010	13 36 44.64	−29 50 33.90							s2
B12-011	13 36 45.31	−29 53 7.80							
B12-012	13 36 45.66	−29 52 21.29							s2
B12-013	13 36 45.93	−29 53 34.40							
B12-014	13 36 46.42	−29 53 42.29							s2
B12-015	13 36 46.94	−29 46 41.70							
B12-016	13 36 47.13	−29 55 31.51							
B12-017	13 36 47.18	−29 53 51.40							
B12-018	13 36 47.22	−29 53 36.89							
B12-019	13 36 47.30	−29 49 3.79							
B12-020	13 36 47.83	−29 51 18.11							s2
B12-021	13 36 47.93	−29 51 46.01							s2
B12-022	13 36 48.11	−29 51 33.91							s2
B12-023	13 36 48.30	−29 52 44.69	CX046	13 36 48.30	−29 52 44.60				s2
B12-024	13 36 48.45	−29 51 42.19							
B12-025	13 36 48.59	−29 52 5.30	X069 (M2X008)	13 36 49.07	−29 52 58.70				s2
B12-026	13 36 48.99	−29 52 54.08							s2
B12-027	13 36 49.12	−29 52 24.89							
B12-028	13 36 49.37	−29 53 19.90							
B12-029	13 36 49.54	−29 51 37.12				R20-030	13 36 49.35	−29 51 36.30	s2
B12-030	13 36 49.60	−29 53 5.71							
B12-031	13 36 49.62	−29 53 13.70							s2
B12-032	13 36 49.63	−29 50 34.40							
B12-033	13 36 49.68	−29 54 4.21							s2
B12-034	13 36 49.72	−29 50 57.08							s2
B12-035	13 36 49.81	−29 53 8.30							s2
B12-036	13 36 49.81	−29 52 16.90	CX053	13 36 49.80	−29 52 17.20				s2
B12-037	13 36 50.12	−29 53 8.70	CX057	13 36 50.09	−29 53 8.40	R20-035	13 36 50.12	−29 53 8.80	s2
B12-038	13 36 50.23	−29 51 24.30							
B12-039	13 36 50.28	−29 52 47.50							s2
B12-040	13 36 50.50	−29 51 49.79							
B12-041	13 36 50.55	−29 53 3.91	CX061	13 36 50.59	−29 53 3.80				

[b] s2: optical SNR was chosen because of the [SII] to Hα ratio, o3: optical SNR was chosen because of [OIII] to Hα ratio, nuc: source lies in the nuclear region of M83

Table 12.2: SNR catalogue (continued).

optical	RA (h,min,s)	DEC (h,′,″)	X-ray	RA (h,min,s)	DEC (h,′,″)	radio	RA (h,min,s)	DEC (h,′,″)	
B12-042	13 36 50.69	−29 52 41.48				R20-036	13 36 50.63	−29 52 40.80	s2
B12-043	13 36 50.76	−29 53 10.61							
B12-044	13 36 50.81	−29 50 18.82							
B12-045	13 36 50.85	−29 52 39.61	CX063	13 36 50.85	−29 52 39.80	R20-039	13 36 50.87	−29 52 39.90	s2
B12-046	13 36 50.92	−29 52 3.79							
B12-047	13 36 50.92	−29 52 58.69	CX064	13 36 50.91	−29 52 59.50				
B12-048	13 36 50.99	−29 52 25.90	CX065 (M2X063)	13 36 50.96	−29 52 25.80	R20-041	13 36 50.98	−29 52 26.00	s2
B12-049	13 36 51.02	−29 53 1.39							
B12-050	13 36 51.23	−29 52 40.69				R20-044	13 36 51.20	−29 52 40.80	
B12-051	13 36 51.32	−29 50 7.12	CX066	13 36 51.10	−29 50 6.90	R20-045	13 36 51.20	−29 50 7.80	
B12-052	13 36 51.43	−29 49 28.20							
B12-053	13 36 51.59	−29 52 50.09							
B12-054	13 36 51.70	−29 52 27.59	CX077	13 36 51.77	−29 52 28.40				
B12-055	13 36 51.98	−29 54 52.42							
B12-056	13 36 52.34	−29 50 33.22							s2
B12-057	13 36 52.40	−29 50 43.91	CX085 (M2X060)	13 36 52.33	−29 50 46.40				s2
B12-058	13 36 52.38	−29 52 5.20							
B12-059	13 36 52.51	−29 49 32.59							
B12-060	13 36 52.64	−29 52 41.48	CX093 (M2X029)	13 36 52.71	−29 52 41.10				
B12-061	13 36 52.78	−29 51 28.51	CX104	13 36 53.19	−29 51 32.60	R20-069 (A026)	13 36 53.20	−29 51 33.10	
B12-062	13 36 52.98	−29 50 23.89							
B12-063	13 36 53.08	−29 52 16.39	CX100	13 36 52.99	−29 52 16.30	R20-066	13 36 52.98	−29 52 16.00	
B12-064	13 36 53.18	−29 52 29.32	CX097	13 36 52.83	−29 52 31.50	R20-061 (A020)	13 36 52.82	−29 52 31.70	
B12-065	13 36 53.23	−29 53 25.30	CX105	13 36 53.23	−29 53 25.20				
B12-066	13 36 53.30	−29 52 42.49	CX107	13 36 53.29	−29 52 42.50	R20-072	13 36 53.30	−29 52 42.10	s2
B12-067	13 36 53.29	−29 52 48.22	CX106	13 36 53.23	−29 52 47.70	R20-065	13 36 52.94	−29 52 48.90	s2
B12-068	13 36 53.32	−29 55 51.38							
B12-069	13 36 53.37	−29 50 38.40				R20-073	13 36 53.37	−29 50 38.30	s2
B12-070	13 36 53.51	−29 52 38.21							
B12-071	13 36 53.63	−29 52 45.91				R20-077	13 36 53.65	−29 52 45.60	
B12-072	13 36 53.77	−29 54 40.90							s2
B12-073	13 36 53.89	−29 48 48.20	CX116 (X077, M2X200)	13 36 53.89	−29 48 48.50	R20-081 (R20-079, A032)	13 36 53.89	−29 48 48.60	s2
B12-074	13 36 54.16	−29 52 9.30	CX119	13 36 54.14	−29 52 9.40				
B12-075	13 36 54.24	−29 50 28.21	CX121	13 36 54.25	−29 50 28.00				
B12-076	13 36 54.34	−29 50 17.59							
B12-077	13 36 54.45	−29 56 0.38							
B12-078	13 36 54.47	−29 50 53.02							s2
B12-079	13 36 54.49	−29 50 26.30	CX124	13 36 54.55	−29 50 26.70	R20-087	13 36 54.47	−29 50 25.70	
B12-080	13 36 54.63	−29 53 4.88	CX126	13 36 54.79	−29 53 9.00	R20-086 (R20-090)	13 36 54.43	−29 53 4.70	
B12-081	13 36 54.63	−29 53 1.21							
B12-082	13 36 54.79	−29 52 59.41	CX127	13 36 54.81	−29 52 59.80	R20-089 (R20-086)	13 36 54.72	−29 52 57.10	
B12-083	13 36 54.83	−29 53 4.70				R20-090	13 36 54.72	−29 53 9.70	
B12-084	13 36 54.87	−29 50 18.60	CX128	13 36 54.87	−29 50 18.70	R20-091	13 36 54.90	−29 50 17.10	s2

Table 12.3: SNR catalogue (continued).

optical	RA (h,min,s)	DEC (h,′,″)	X-ray	RA (h,min,s)	DEC (h,′,″)	radio	RA (h,min,s)	DEC (h,′,″)	
B12-085	13 36 54.84	−29 49 53.62							
B12-086	13 36 54.94	−29 47 45.89							
B12-087	13 36 55.03	−29 52 39.61	CX129	13 36 55.03	−29 52 39.40	R20-092	13 36 55.03	−29 52 39.60	s2
B12-088	13 36 55.03	−29 51 24.91							
B12-089	13 36 55.06	−29 53 4.49	CX131 (M2X051)	13 36 55.06	−29 53 4.50	R20-093 (R20-090)	13 36 55.13	−29 53 9.20	s2
B12-090	13 36 55.13	−29 50 40.31	CX134	13 36 55.16	−29 50 39.90				
B12-091	13 36 55.22	−29 53 4.99	M2X051	13 36 55.06	−29 53 4.50				s2
B12-092	13 36 55.31	−29 50 37.21				R20-095	13 36 55.27	−29 50 51.10	s2
B12-093	13 36 55.35	−29 50 53.70	CX136	13 36 55.36	−29 50 53.50				
B12-094	13 36 55.32	−29 49 56.71							
B12-095	13 36 55.41	−29 48 39.20	CX137	13 36 55.37	−29 48 40.70				
B12-096	13 36 55.47	−29 53 3.52				R20-098	13 36 55.54	−29 53 3.10	s2
B12-097	13 36 55.48	−29 52 43.72							
B12-098	13 36 55.62	−29 53 3.59	CX139	13 36 55.56	−29 53 3.50	R20-098	13 36 55.54	−29 53 3.10	s2
B12-099	13 36 55.62	−29 47 37.39							
B12-100	13 36 55.69	−29 49 25.10							s2
B12-101	13 36 55.80	−29 51 19.69							
B12-102	13 36 55.83	−29 53 9.20							
B12-103	13 36 55.91	−29 53 10.90							
B12-104	13 36 56.06	−29 56 5.71							s2
B12-105	13 36 56.11	−29 49 35.00							
B12-106	13 36 56.23	−29 52 55.20	CX141	13 36 56.23	−29 52 55.10	R20-103	13 36 56.23	−29 52 55.00	s2
B12-107	13 36 56.27	−29 53 13.42							
B12-108	13 36 56.36	−29 49 32.30				R20-107	13 36 56.44	−29 49 33.50	s2
B12-109	13 36 56.81	−29 49 49.69	CX149	13 36 56.84	−29 49 50.30				s2
B12-110	13 36 56.82	−29 49 24.82							
B12-111	13 36 56.92	−29 54 10.58							
B12-112	13 36 57.16	−29 53 33.68	X081 (M2X013)	13 36 57.22	−29 53 38.30	R20-112	13 36 57.15	−29 53 33.60	s2
B12-113	13 36 57.83	−29 48 5.80							
B12-114	13 36 57.97	−29 48 12.71							
B12-115	13 36 57.88	−29 53 2.80	CX159 (M2X068)	13 36 57.88	−29 53 2.80				s2
B12-116	13 36 58.07	−29 53 44.92							
B12-117	13 36 58.55	−29 48 19.69	CX166	13 36 58.56	−29 48 20.00				s2
B12-118	13 36 58.72	−29 51 0.61	CX172 (M2X032)	13 36 58.71	−29 51 0.60				s2
B12-119	13 36 59.00	−29 52 56.78							s2
B12-120	13 36 59.01	−29 53 1.39							
B12-121	13 36 59.10	−29 53 43.40							
B12-122	13 36 59.33	−29 55 8.90	CX183	13 36 59.33	−29 55 8.80	R20-128	13 36 59.33	−29 55 8.90	s2
B12-123	13 36 59.34	−29 48 37.70	CX184	13 36 59.36	−29 48 37.40	R20-129	13 36 59.38	−29 48 36.80	s2, nuc
B12-124	13 36 59.50	−29 52 3.90	CX186	13 36 59.51	−29 52 4.00	R20-130	13 36 59.55	−29 52 3.40	s2
B12-125	13 36 59.47	−29 49 16.61							
B12-126	13 36 59.68	−29 50 32.78							
B12-127	13 36 59.85	−29 55 26.00	CX195 (M2X099)	13 36 59.83	−29 55 26.00				s2

Table 12.4: SNR catalogue (continued).

optical	RA (h,min,s)	DEC (h,′,″)	X-ray	RA (h,min,s)	DEC (h,′,″)	radio	RA (h,min,s)	DEC (h,′,″)	
B12-128	13 37 0.01	−29 48 33.70							s2
B12-129	13 37 0.03	−29 54 16.88	CX199 (M2X085)	13 37 0.01	−29 54 17.10				s2
B12-130	13 37 0.09	−29 48 40.28				R20-137	13 37 0.09	−29 48 40.90	
B12-131	13 37 0.16	−29 48 10.12	CX205	13 37 0.18	−29 48 10.20				s2
B12-132	13 37 0.34	−29 51 20.70							s2
B12-133	13 37 0.40	−29 53 22.88	CX215 (X092, M2X009)	13 37 0.37	−29 53 23.10				nuc
B12-134	13 37 0.68	−29 54 26.71							s2
B12-135	13 37 0.69	−29 52 22.01				R20-145	13 37 0.68	−29 52 21.50	s2
B12-136	13 37 0.73	−29 53 23.71	M2X009	13 37 0.37	−29 53 23.10				
B12-137	13 37 1.02	−29 50 56.29	CX235	13 37 1.03	−29 50 56.50	R20-150	13 37 1.00	−29 50 56.10	s2
B12-138	13 37 1.06	−29 54 15.91							
B12-139	13 37 1.16	−29 57 10.69							
B12-140	13 37 1.51	−29 50 14.71				R20-156	13 37 1.50	−29 50 1.50	
B12-141	13 37 1.55	−29 49 58.91	CX249	13 37 1.57	−29 49 59.00				s2
B12-142	13 37 1.66	−29 54 10.12	CX253	13 37 1.67	−29 54 10.00				
B12-143	13 37 1.71	−29 51 13.39	CX256	13 37 1.73	−29 51 13.40	R20-157	13 37 1.72	−29 51 13.20	s2
B12-144	13 37 1.72	−29 54 40.39	CX255	13 37 1.70	−29 54 40.60				
B12-145	13 37 2.04	−29 52 49.58	PNX033	13 37 1.76	−29 52 49.06				
B12-146	13 37 2.07	−29 51 58.28							s2
B12-147	13 37 2.21	−29 49 52.39	CX261	13 37 2.21	−29 49 52.50	R20-159	13 37 2.23	−29 49 52.70	s2
B12-148	13 37 2.32	−29 50 7.01	CX262	13 37 2.31	−29 50 7.30				s2
B12-149	13 37 2.41	−29 54 32.90							
B12-150	13 37 2.42	−29 51 26.10	CX265 (M2X026)	13 37 2.42	−29 51 26.10	R20-160	13 37 2.42	−29 51 26.00	s2
B12-151	13 37 3.02	−29 49 45.52	CX272	13 37 3.02	−29 49 45.50	R20-165	13 37 3.02	−29 49 45.10	s2
B12-152	13 37 3.48	−29 50 46.72							
B12-153	13 37 3.88	−29 49 43.00				R20-174	13 37 3.91	−29 49 43.00	
B12-155	13 37 4.14	−29 53 16.19							
B12-156	13 37 4.41	−29 49 38.60	CX287	13 37 4.41	−29 49 38.70	R20-177	13 37 4.40	−29 49 38.60	s2
B12-157	13 37 4.46	−29 53 47.69							
B12-159	13 37 4.50	−29 49 35.51	CX288	13 37 4.52	−29 49 35.40	R20-177	13 37 4.40	−29 49 38.60	s2
B12-160	13 37 4.71	−29 55 34.79	CX292	13 37 4.66	−29 55 34.10	R20-180	13 37 4.71	−29 55 34.80	s2
B12-161	13 37 4.76	−29 53 53.59							
B12-162	13 37 4.81	−29 50 6.79							
B12-163	13 37 4.85	−29 49 41.99							s2
B12-164	13 37 4.96	−29 50 16.30							
B12-165	13 37 5.58	−29 54 56.30							
B12-166	13 37 5.80	−29 52 45.98							
B12-167	13 37 5.87	−29 55 4.01							
B12-168	13 37 6.00	−29 50 4.20							
B12-169	13 37 6.04	−29 55 14.30	CX310 (M2X117)	13 37 6.02	−29 55 14.40	R20-191	13 37 6.03	−29 55 15.00	s2
B12-170	13 37 6.16	−29 54 43.49	CX311 (M1X085)	13 37 6.17	−29 54 44.20				s2
B12-171	13 37 6.44	−29 50 25.01	CX313 (M1X066)	13 37 6.44	−29 50 25.40				s2
B12-172	13 37 6.45	−29 54 27.29				R20-192	13 37 6.41	−29 54 27.20	s2

Table 12.5: SNR catalogue (continued).

optical	RA (h,min,s)	DEC (h,′,″)	X-ray	RA (h,min,s)	DEC (h,′,″)	radio	RA (h,min,s)	DEC (h,′,″)	
B12-173	13 37 6.45	−29 50 6.22							
B12-174	13 37 6.64	−29 53 34.01				R20-193	13 37 6.64	−29 53 32.80	
B12-174a	13 37 6.65	−29 53 32.60	CX316	13 37 6.64	−29 53 32.70	R20-193	13 37 6.64	−29 53 32.80	o3
B12-175	13 37 6.82	−29 49 26.18				R20-197	13 37 6.80	−29 49 23.70	
B12-176	13 37 7.00	−29 54 16.20							
B12-177	13 37 6.99	−29 49 7.90	CX319	13 37 7.03	−29 49 8.10				
B12-178	13 37 7.08	−29 53 21.01	CX320	13 37 7.07	−29 53 20.90				s2
B12-179	13 37 7.11	−29 51 1.58	CX321 (X114, M2X007)	13 37 7.11	−29 51 1.60				s2
B12-180	13 37 7.47	−29 51 33.41	CX326 (X116)	13 37 7.48	−29 51 33.40	R20-204	13 37 7.47	−29 51 33.80	s2
B12-181	13 37 7.50	−29 54 16.20							
B12-182	13 37 7.57	−29 52 19.20	M1X060	13 37 7.29	−29 52 22.49				
B12-183	13 37 7.69	−29 51 10.12				R20-206	13 37 7.68	−29 51 12.70	s2
B12-184	13 37 7.71	−29 53 1.28	CX333	13 37 8.21	−29 52 57.40	R20-212 (A090)	13 37 8.13	−29 52 56.40	s2
B12-185	13 37 7.80	−29 54 12.20							
B12-186	13 37 7.92	−29 49 20.10	CX330 (M1X079)	13 37 7.92	−29 49 20.30	R20-210	13 37 7.97	−29 49 20.80	
B12-187	13 37 8.01	−29 51 16.49				R20-209	13 37 7.93	−29 51 18.20	s2
B12-188	13 37 8.10	−29 52 21.50							
B12-189	13 37 8.16	−29 53 20.69							
B12-190	13 37 8.48	−29 52 1.99	CX338	13 37 8.48	−29 52 1.70	R20-216	13 37 8.49	−29 52 2.60	s2
B12-191	13 37 8.57	−29 51 35.21	CX339	13 37 8.57	−29 51 35.00				
B12-192	13 37 8.65	−29 51 53.39							
B12-193	13 37 8.76	−29 51 37.51	CX342	13 37 8.77	−29 51 37.60	R20-221	13 37 8.76	−29 51 37.60	s2
B12-194	13 37 9.05	−29 51 33.30				R20-224	13 37 9.05	−29 51 33.40	s2
B12-195	13 37 9.23	−29 51 33.98	CX348	13 37 9.25	−29 51 33.80	R20-227	13 37 9.27	−29 51 33.60	
B12-196	13 37 9.69	−29 53 30.19							
B12-197	13 37 10.08	−29 51 28.19	CX350	13 37 10.06	−29 51 28.00	R20-233	13 37 10.10	−29 51 28.90	s2
B12-198	13 37 10.19	−29 50 18.10				R20-233	13 37 10.10	−29 51 28.90	
B12-199	13 37 10.31	−29 51 29.02	CX352	13 37 10.36	−29 51 29.40	R20-234	13 37 10.87	−29 49 55.80	s2
B12-200	13 37 10.78	−29 49 56.50				R20-234	13 37 10.87	−29 49 55.80	s2
B12-201	13 37 10.80	−29 51 44.60							
B12-202	13 37 10.93	−29 49 53.00	CX353	13 37 10.99	−29 50 46.50	R20-234	13 37 10.87	−29 49 55.80	s2
B12-203	13 37 10.97	−29 50 46.28							s2
B12-204	13 37 11.11	−29 53 17.09							s2
B12-205	13 37 11.34	−29 54 19.40							s2
B12-206	13 37 11.47	−29 51 41.40	CX356	13 37 11.50	−29 51 41.50				s2
B12-207	13 37 11.46	−29 50 13.60	CX355	13 37 11.48	−29 50 13.70	R20-238	13 37 11.48	−29 50 13.70	s2
B12-208	13 37 11.63	−29 51 39.49							s2
B12-209	13 37 11.88	−29 52 15.71	CX358	13 37 11.88	−29 52 15.50				s2
B12-210	13 37 12.46	−29 50 20.11	CX364 (M2X110)	13 37 12.45	−29 50 20.20				s2
B12-211	13 37 12.81	−29 50 12.01	CX368	13 37 12.81	−29 50 12.30				
B12-212	13 37 12.84	−29 54 38.70							
B12-213	13 37 13.08	−29 51 18.22							
B12-214	13 37 14.03	−29 52 54.30				R20-247	13 37 14.02	−29 52 54.60	s2

Table 12.6: SNR catalogue (continued).

optical	RA (h,min,s)	DEC (h,′,″)	X-ray	RA (h,min,s)	DEC (h,′,″)	radio	RA (h,min,s)	DEC (h,′,″)	
B12-215	13 37 13.97	−29 51 51.08	M2X072	13 37 14.36	−29 51 48.27				s2
B12-216	13 37 14.36	−29 50 6.40							
B12-217	13 37 14.43	−29 50 21.19							
B12-218	13 37 14.68	−29 50 34.01				R20-249	13 37 14.79	−29 50 36.80	
B12-219	13 37 14.84	−29 54 58.61							s2
B12-220	13 37 16.02	−29 53 3.98							s2
B12-221	13 37 17.20	−29 51 53.39	CX389 (X130, M2X087)	13 37 17.21	−29 51 53.30	R20-256	13 37 17.20	−29 51 53.80	s2
B12-222	13 37 17.27	−29 53 25.01							s2
B12-223	13 37 17.43	−29 51 53.89	CX391 (M2X087)	13 37 17.40	−29 51 54.00	R20-258	13 37 17.43	−29 51 54.30	s2
B12-224	13 37 17.49	−29 53 35.81							
B12-225	13 37 18.74	−29 53 50.50							
B12-309	13 36 49.90	−29 52 59.09	CX054	13 36 49.92	−29 52 59.40				
B12-310	13 36 50.24	−29 50 36.89							
B12-311	13 36 52.27	−29 54 20.92	CX110 (X076)	13 36 53.61	−29 56 0.90	R20-076	13 36 53.62	−29 56 1.10	o3
B12-312	13 36 53.60	−29 56 0.82							o3
B12-313	13 36 55.05	−29 54 54.40							
B12-314	13 36 55.27	−29 54 2.81	X135 (X135)	13 36 55.20	−29 54 3.10				o3
B12-316	13 36 58.04	−29 49 1.99							o3
B12-318	13 36 59.03	−29 54 58.61							o3
B12-319	13 36 59.30	−29 54 58.21							
B12-320	13 36 59.45	−29 54 34.70							o3
B12-321	13 37 1.27	−29 51 59.90	CX243	13 37 1.28	−29 52 0.10	R20-154 (R20-152)	13 37 1.33	−29 51 58.50	o3, nuc
B12-324	13 37 3.58	−29 49 40.69	CX279	13 37 3.58	−29 49 40.80	R20-172 (A073)	13 37 3.58	−29 49 40.90	o3
B12-327	13 37 5.88	−29 49 11.32							
B12-328	13 37 6.97	−29 54 57.31							
B12-329	13 37 7.09	−29 49 13.51							
B12-333	13 37 8.64	−29 52 42.82	CX341	13 37 8.69	−29 52 43.40				o3
B12-334	13 37 10.19	−29 48 59.29							
B12-336	13 37 12.08	−29 50 57.08	CX360	13 37 12.06	−29 50 57.10				o3
B12-338	13 37 12.81	−29 54 44.32							
B12-344	13 37 17.79	−29 51 55.40							o3
B14-03	13 36 50.12	−29 52 43.72				R20-034	13 36 50.07	−29 52 43.70	
B14-07	13 36 51.19	−29 50 42.30	CX067	13 36 51.19	−29 50 42.30	R20-043 (A015)	13 36 51.15	−29 50 42.20	s2
B14-08	13 36 51.48	−29 52 33.20							
B14-09	13 36 51.53	−29 53 0.89	CX078	13 36 51.80	−29 53 1.60	R20-048 (R20-052, A018)	13 36 51.53	−29 53 0.30	s2
B14-10	13 36 51.81	−29 52 1.88							
B14-13	13 36 53.73	−29 48 51.30							
B14-19	13 36 58.64	−29 51 6.52	CX170 (X083, M2X032)	13 36 58.66	−29 51 6.70	R20-079	13 36 53.75	−29 48 49.70	s2
B14-20	13 36 58.90	−29 52 26.29	CX176	13 36 58.91	−29 52 25.60				nuc s2
B14-22	13 36 59.17	−29 51 47.92	CX181	13 36 59.19	−29 51 48	R20-126	13 36 59.17	−29 51 48.20	nuc
B14-23	13 36 59.32	−29 48 36.50	CX184	13 36 59.36	−29 48 37.40	R20-129	13 36 59.38	−29 48 36.80	
B14-24	13 36 59.44	−29 48 37.00	CX184	13 36 59.36	−29 48 37.40	R20-129	13 36 59.38	−29 48 36.80	
B14-25	13 36 59.79	−29 48 37.91							

Table 12.7: SNR catalogue (continued).

optical	RA (h,min,s)	DEC (h,′,″)	X-ray	RA (h,min,s)	DEC (h,′,″)	radio	RA (h,min,s)	DEC (h,′,″)	
B14-27	13 37 0.04	−29 52 1.88	CX202	13 37 0.06	−29 52 2.00	R20-138	13 37 0.12	−29 52 2.10	nuc
B14-28	13 37 0.07	−29 52 8.80				R20-136	13 37 0.05	−29 52 16.40	
B14-29	13 37 0.34	−29 52 5.41	CX212	13 37 0.33	−29 52 5.50	R20-138 (R20-146)	13 37 0.12	−29 52 2.10	nuc
B14-30	13 37 0.41	−29 52 6.20				R20-146 (R20-141)	13 37 0.71	−29 52 7.50	nuc
B14-31	13 37 0.41	−29 52 22.58	CX219	13 37 0.44	−29 52 23.00	R20-142	13 37 0.42	−29 52 22.60	nuc
B14-32	13 37 0.55	−29 52 6.49	CX224	13 37 0.57	−29 52 4.00	R20-146 (R20-141)	13 37 0.71	−29 52 7.50	nuc
B14-34	13 37 0.88	−29 52 8.40							
B14-36	13 37 1.07	−29 51 41.62				R20-147	13 37 0.89	−29 51 43.40	nuc
B14-37	13 37 1.99	−29 51 51.41							
B14-39	13 37 1.61	−29 52 1.88	CX250	13 37 1.61	−29 52 2.20	R20-154	13 37 1.33	−29 51 58.50	nuc
B14-42	13 37 2.89	−29 48 39.10							s2
B14-44	13 37 3.14	−29 54 16.88							
B14-45	13 37 3.40	−29 54 2.48	CX275	13 37 3.46	−29 54 1.70	R20-171 (A072)	13 37 3.44	−29 54 2.30	
B14-47	13 37 5.02	−29 55 21.68							
B14-49	13 37 5.88	−29 50 45.49				R20-188	13 37 5.86	−29 50 45.00	s2
B14-50	13 37 6.23	−29 55 5.09							
B14-51	13 37 6.99	−29 51 9.61							
B14-54	13 37 8.33	−29 50 56.29	CX336	13 37 8.31	−29 50 56.30				s2
B14-55	13 37 8.40	−29 52 47.71							
B14-56	13 37 8.42	−29 52 10.20				R20-214 (R20-217)	13 37 8.30	−29 52 11.70	
B14-58	13 37 9.31	−29 50 58.49				R20-228	13 37 9.28	−29 51 1.00	
B14-60	13 37 13.07	−29 51 38.48							
B14-61	13 37 13.33	−29 51 35.89							
D10-1-01	13 37 4.12	−29 51 3.82	M2X007	13 37 7.01	−29 51 0.80				o3
D10-1-02	13 37 6.97	−29 50 57.08							o3
D10-17	13 37 4.88	−29 52 18.59							s2
D10-38	13 37 10.36	−29 51 33.91							s2
D10-40	13 37 10.84	−29 52 44.51							s2
D10-N-02	13 37 0.21	−29 51 58.39	CX188	13 36 59.65	−29 51 55.80	R20-140	13 37 0.32	−29 51 51.10	
D10-N-03	13 37 0.22	−29 52 6.20	CX207	13 37 0.22	−29 52 6.50	R20-138	13 37 0.34	−29 52 2.10	nuc
D10-N-05	13 37 0.39	−29 51 58.72	CX216 (X090)	13 37 0.42	−29 51 59.80	R20-141	13 37 0.41	−29 52 0.60	nuc
D10-N-06	13 37 0.40	−29 52 1.70				R20-141	13 37 0.41	−29 52 0.60	nuc
D10-N-08	13 37 0.55	−29 51 58.79	CX223	13 37 0.55	−29 51 59.20	R20-141 (R20-144)	13 37 0.41	−29 52 0.60	nuc
D10-N-09	13 37 0.60	−29 52 8.80	CX222	13 37 0.55	−29 52 10.30	R20-146	13 37 0.71	−29 52 7.50	nuc
D10-N-10	13 37 0.65	−29 51 59.40							
D10-N-11	13 37 0.68	−29 51 57.10	CX231	13 37 0.71	−29 51 56.80	R20-144 (R20-148)	13 37 0.59	−29 51 56.40	nuc
D10-N-12	13 37 0.70	−29 51 59.90	CX229 (X093)	13 37 0.68	−29 52 0.50	R20-144	13 37 0.59	−29 51 56.40	nuc
D10-N-14(1)	13 37 0.93	−29 51 54.11				R20-148	13 37 0.91	−29 51 55.90	nuc
D10-N-14(2)	13 37 0.94	−29 51 54.61				R20-148	13 37 0.91	−29 51 55.90	nuc
D10-N-14(3)	13 37 0.97	−29 51 53.60				R20-151 (R20-148)	13 37 1.12	−29 51 52.20	nuc
D10-N-15	13 37 0.94	−29 51 55.91	CX233	13 37 0.89	−29 51 56.00	R20-148	13 37 0.91	−29 51 55.90	nuc
D10-N-17	13 37 1.17	−29 51 57.31	CX241	13 37 1.19	−29 51 57.30	R20-154 (R20-148)	13 37 1.33	−29 51 58.50	nuc
D10-N-18	13 37 1.31	−29 51 57.38				R20-154	13 37 1.33	−29 51 58.50	nuc

B. Data processing – commands

The following subsections list the commands used for the XMM data processing based on the threads in [16]. Text in the `typewriter`-style denote commands and red text highlights the outputs of the corresponding commands. Normal-styled text is simply additional information/comments on some commands and outputs.

B.1. SAS start-up

```
setenv SAS_DIR /some_dir/xmmsas_202010_1931
setenv SAS_CCFPATH /ccf
setenv SAS_ODF /home/user/xmm_obs/0099280201 cifbuild
```
 – *output:* ccf.cif
```
setenv SAS_CCF 'pwd'/ccf.cif
odfingest
```
 – *output:* 2868_0761620101_SCX00000SUM.SAS
```
setenv SAS_ODF 'pwd'/'ls -1 *SUM.SAS'
```

The directory paths are exemplary. *0761620101* in the command `odfingest` is the ID of the observation I analyzed.

B.2. Creating concatenated event files

MOS

```
emproc
```
output of `emproc`:
2868_0761620101_AttHk.ds, 2868_0761620101_EMOS1_S001_01_Badpixels.ds and 2868_0761620101_EMOS1_S001_ImagingEvts.ds

Using `emproc` results conceptionally in the same output for *MOS2*, except 'EMOS1' is replaced by 'EMOS2' and 'S001' is replaced by 'S002'. The file containing the bad pixels is just an example. There are more bad pixel files, which are numbered, hence the '01' in the name of the file indicates it is the first bad pixel file.

PN

```
epproc
```
output of `epproc`:
2868_0761620101_AttHk.ds, 2868_0761620101_EPN_S003_01_Badpixels.ds and 2868_0761620101_EPN_S003_ImagingEvts.ds

The information on the bad pixel files from above also holds for the *PN* camera.

B.3. Filtering

MOS

```
evselect table=2868_0761620101_EMOS1_S001_ImagingEvts.ds expression=\
'#XMMEA_EM && (PATTERN<=12)' updateexposure=yes filterexposure=yes \
withfilteredset=true destruct=yes keepfilteroutput=true \
filteredset=rateEPIC_MOS1.fits
```
output of evselect: rateEPIC_MOS1.fits

```
tabgtigen table=rateEPIC_MOS1.fits expression='RATE<=0.35' \
gtiset=EPICgti_MOS1.fits
```
output of tabtigen: EPICgti_MOS1.fits

```
evselect table=EPICgti_MOS1.fits withfilteredset=Y \
filteredset=MOS1clean.fits destruct=Y keepfilteroutput=T expression=\
'#XMMEA_EM && gti(EPICgti_MOS1.fits,TIME) && (PI>150)'
```
output of evselect: MOS1clean.fits

Again, conceptionally the same commands can be used for *MOS2*, one just has to change the input file name and the desired output file name.

PN

```
evselect table=2868_0761620101_EP_S003_ImagingEvts.ds expression=\
'#XMMEA_EP\ && (PATTERN<=4)' updateexposure=yes filterexposure=yes \
withfilteredset=true destruct=yes keepfilteroutput=true \
filteredset=rateEPIC_PN.fits
```
output of evselect: rateEPIC_PN.fits

```
tabgtigen table=rateEPIC_PN.fits expression='RATE<=0.4' \
gtiset=EPICgti_PN.fits
```
output of tabtigen: EPICgti_PN.fits

```
evselect table=EPICgti_PN.fits withfilteredset=Y \
filteredset=PNclean.fits destruct=Y keepfilteroutput=T expression=\
'#XMMEA_EP && gti(EPICgti_PN.fits,TIME) && (PI>150)'
```
output of evselect: PNclean.fits

B.4. Creating images and event files

MOS

```
evselect table=MOS1clean.fits:EVENTS imagebinning='binSize' \
imageset='m1_image_b1.fits' withimageset=yes xcolumn='X' ycolumn='Y' \
ximagebinsize=40 yimagebinsize=40 expression=\
'#XMMEA_EM&&(PI in [300:700])&&(PATTERN in [0:12])&&(FLAG==0)'
```
output of ***evselect:*** m1_image_b1.fits

Replacing the energy interval with the other two bands yields conceptionally the same files, except the 'b1' is changed to 'b2' and 'b3'. Executing this command for the entire energy range will result in m1_image_full.fits.

```
edetect_chain imagesets='"m1_image_b1.fits" "m1_image_b2.fits" \
"m1_image_b3.fits"' eventsets=MOS1clean.evt attitudeset=\
2868_0761620101_AttHk.ds pimin='300 700 1100' pimax='700 1100 4200' \
ecf='1.75 1.79 2.02' eboxl_list='m1_eboxlist_l.fits' \
eboxm_list='m1_eboxlist_m.fits' esp_nsplinenodes=16 \
eml_list='m1_emllist.fits' esen_mlmin=15
```
output of ***edetect_chain:***
m1_eboxlist_l.fits, m1_eboxlist_m.fits and m1_emllist.fits

The same commands can be used for *MOS2*, when changing input and output file names.

PN

```
evselect table=PNclean.fits:EVENTS imagebinning='binSize' \
imageset='pn_image_b1.fits' withimageset=yes xcolumn='X' ycolumn='Y' \
ximagebinsize=40 yimagebinsize=40 expression=\
'#XMMEA_EP&&(PI in [300:700])&&(PATTERN in [0:4])&&(FLAG==0)'
```
output of ***evselect:*** pn_image_b1.fits

Replacing the energy interval with the other two bands yields conceptionally the same files, except the 'b1' is changed to 'b2' and 'b3'. Executing this command for the entire energy range will result in pn_image_full.fits.

```
edetect_chain imagesets='"pn_image_b1.fits" "pn_image_b2.fits" \
"pn_image_b3.fits"' eventsets=PNclean.fits attitudeset=\
2868_0761620101_AttHk.ds pimin='300 700 1100' pimax='700 1100 4200' \
ecf='10.22 8.87 5.62' eboxl_list='pn_eboxlist_l.fits' \
eboxm_list='pn_eboxlist_m.fits' esp_nsplinenodes=16 \
eml_list='pn_emllist.fits' esen_mlmin=15
```
output of ***edetect_chain:***
pn_eboxlist_l.fits, pn_eboxlist_m.fits and pn_emllist.fits.

B.5. Spectrum extraction

```
evselect table=MOS1clean.fits withspectrumset=yes spectrumset=\
MOS1source_spectrum.fits energycolumn=PI spectralbinsize=5 \
withspecranges=yes specchannelmin=0 specchannelmax=11999 \
expression='#XMMEA_EM && (PATTERN<=12) && ((X,Y) \
IN circle(30360.5,28400.5,640))'
```
output of evselect: MOS1source_spectrum.fits

```
evselect table=MOS1clean.fits withspectrumset=yes spectrumset=\
MOS1background_spectrum.fits energycolumn=PI spectralbinsize=5 \
withspecranges=yes specchannelmin=0 specchannelmax=11999 \
expression='#XMMEA_EM && (PATTERN<=12) && ((X,Y) \
IN circle(30720.5,26360.5,640))'
```
output of evselect: MOS1background_spectrum.fits

The circular area is an examplary area around the source and in the background with the same radius (in physical coordinates). The commands above and the ones below can also be executed for *MOS2*, when changing the file names to the names corresponding to *MOS2*. Changing the *specchannelmax* parameter to 20479 and 'PATTERN<=12' to 'PATTERN<=4' as well as input and output file names, one can also use all spectrum extraction commands for the *PN* camera.

```
backscale spectrumset=MOS1source_spectrum.fits badpixlocation=\
MOS1clean.fits
```

```
backscale spectrumset=MOS1background_spectrum.fits badpixlocation=\
MOS1clean.fits
```

```
rmfgen spectrumset=MOS1source_spectrum.fits rmfset=MOS1.rmf
```
output of rmfgen: MOS1.rmf

```
arfgen spectrumset=MOS1source_spectrum.fits arfset=MOS1.arf withrmfset=\
yes rmfset=MOS1.rmf badpixlocation=MOS1clean.fits detmaptype=psf
```
output of arfgen: MOS1.arf

```
specgroup spectrumset=MOS1source_spectrum.fits mincounts=30 \
oversample=3 rmfset=MOS1.rmf arfset=MOS1.arf backgndset=\
MOS1background_spectrum.fits groupedset=MOS1_spectrum_grp.fits
```
output of specgroup: MOS1_spectrum_grp.fits

Eigenständigkeitserklärung

Hiermit versichere ich, dass ich die vorliegende Bachelorarbeit selbstständig verfasst habe. Ich versichere, dass ich keine anderen als die angegebenen Quellen benutzt und alle wörtlich oder sinngemäß aus anderen Werken übernommenen Aussagen als solche gekennzeichnet habe, und dass die eingereichte Arbeit weder vollständig noch in wesentlichen Teilen Gegenstand eines anderen Prüfungsverfahrens gewesen ist.

Erlangen, den 12. April 2022

Ort, Datum

Maximilian Schroth